University of New Mexico
UNM Digital Repository

Electrical and Computer Engineering ETDs | Engineering ETDs

9-9-2007

Microscopy study of extreme lattice mismatched heteroepitaxy using interfacial misfit arrays

Shenghong Huang

Follow this and additional works at: https://digitalrepository.unm.edu/ece_etds

Recommended Citation
Huang, Shenghong. "Microscopy study of extreme lattice mismatched heteroepitaxy using interfacial misfit arrays." (2007).
https://digitalrepository.unm.edu/ece_etds/121

This Dissertation is brought to you for free and open access by the Engineering ETDs at UNM Digital Repository. It has been accepted for inclusion in Electrical and Computer Engineering ETDs by an authorized administrator of UNM Digital Repository. For more information, please contact disc@unm.edu.

MICROSCOPY STUDY OF EXTREME LATTICE MISMATCHED HETEROEPITAXY USING INTERFACIAL MISFIT ARRAYS

BY

SHENGHONG HUANG

B.S., Material Science, Southern Institute of Metallurgy, 1991
M.S., Material Science, Northeastern University, 1994
M.S., Electrical Engineering, University of New Mexico, 2003

COMMITTEE CHAIR: DIANA HUFFAKER

DISSERTATION

Submitted in Partial Fulfillment of the
Requirements for the Degree of

Doctor of Philosophy
Engineering

The University of New Mexico
Albuquerque, New Mexico

July 2007

© 2007, Shenghong Huang

All rights Reserved

Dedicated to my wife, ***Jing***, my sons, ***David*** and ***Kevin***,

and my parents.

ACKNOWLEDGMENTS

I would like to extend my deepest thanks to my advisor, Prof. Diana Huffaker, for encouragement, guidance, insight and support throughout the duration of my Ph.D program. She has always kept giving me warm and helpful guidance and encouragements on my research. Her preciseness, sagacity, acuity and endless enthusiasm on research make a good example to me to be a great scientist.

I would also thank my committee members, Prof. Sanjay Krishna, Prof. Ralph Dawson, Dr. Peng Li and Dr. Andreas Stintz for reading and commenting on my dissertation.

I would like to thank Dr. Peng Li for his help with the TEM experiment and analysis. His patience and input in my research are greatly appreciated.

I would like to thank my group members for their support. I am extremely grateful for their friendship and spirit of teamwork.

I would like to thank my wife, Jing, my parents for their affectionate support and encouragement during this period.

Finally, I would like to thank all of my friends at Center for High Technology Materials of University of New Mexico because all of you enriched my life and made my experience here extraordinary.

MICROSCOPY STUDY OF EXTREME LATTICE MISMATCHED HETEROEPITAXY USING INTERFACIAL MISFIT ARRAYS

BY

SHENGHONG HUANG

B.S., Material Science, Southern Institute of Metallurgy, 1991
M.S., Material Science, Northeastern University, 1994
M.S., Electrical Engineering, University of New Mexico, 2003

ABSTRACT OF DISSERTATION

Submitted in Partial Fulfillment of the
Requirements for the Degree of

Doctor of Philosophy
Engineering

The University of New Mexico
Albuquerque, New Mexico

July 2007

MICROSCOPY STUDY OF EXTREME LATTICE MISMATCHED HETEROEPITAXY USING INTERFACIAL MISFIT ARRAYS

by

Shenghong Huang

B.S., Material Science, Southern Institute of Metallurgy, 1991
M.S., Material Science, Northeastern University, 1994
M.S., Electrical Engineering, University of New Mexico, 2003
Ph.D., Engineering, University of New Mexico, 2007

ABSTRACT

The Sb-bearing compounds offer a wide range of electronic bandgaps, bandgap offsets and electronic barriers along with the extremely high electron mobility and therefore enable a variety of high speed, low power electronic devices and infrared light sources. Therefore, lattice-mismatched epitaxy of Sb-based materials on GaAs and Si substrates has attracted considerable attention. However, due to material growth issues such as large lattice mismatch, anti-phase domains and thermal expansion coefficient mismatch, the material relieves strain energy through misfit dislocations, defects and often threading dislocations, which vertically propagate to active regions of devices, thus leads to non-radiative recombination and damages device performance.

The majority of the work done in this field has been focused on the interfacial misfit (IMF) array based growth mode between GaAs and GaSb, and AlSb on Si substrate. Since the formation of an IMF array does not proceed through the critical thickness method, but instead makes use of atomic arrangements on the surface of substrate to spontaneously relieve the high strain energy between the epi-layer and substrate. Thus this growth mode allows us to grow highly mismatched and low defect density epi-layer material.

In this research, not only have we demonstrated that an IMF array can be formed to fully relieve strain energy at the compressive GaSb/GaAs interface, but also verified that an IMF array can be obtained in the tensile GaAs/GaSb interface once the reaction of the As_2 with GaSb surface is suppressed. Meanwhile, the IMF growth mode has also been applied for obtaining high quality AlSb epilayers monolithically on 5° miscut Si (100) substrate. We attribute the success of AlSb growth on 5° miscut Si (100) surface to both the step doubling-atom mechanism in combination with the strong Al-Sb atomic bond. The AlSb bulk materials with low dislocation density and strain-relieved properties generated by the growth conditions can provide a promising technology for the monolithic integration of III-V devices on Si substrate. Finally, We have demonstrated the ability to control either an IMF or a Stranski-Krastanov (SK) growth mode to grow GaSb QDs on GaAs substrates by varying V/III ratio. A high V/III ratio such as 10:1 produces IMF growth mode, while a low V/III ratio of 1:1 favors SK growth mode.

TABLE OF CONTENTS

Acknowledgements ..... **v**

Abstrate ..... **vii**

Table of Contents ..... **ix**

List of Figures ..... **xii**

List of Tables ..... **xvii**

Chapter 1 Overview of III-V materials on GaAs and Si technology **1**

1.1 The issues for large mismatched III-Sb material growth. 1

1.2 The concept of interfacial misfit array 3

1.3 Objective for the work 4

References for chapter one 5

Chapter 2 Self-Assembled Interfacial Misfit Dislocation Arrays between GaAs and GaSb **6**

2.1 Formation of compressive GaSb/GaAs IMF interface. 6

2.1.1 Introduction. 6

2.1.2 Experimental processes. 8

2.1.3 TEM characterization techniques. 9

2.1.4 Results and discussions. 16

2.1.5 Summary. 22

2.2 Formation of tensile GaAs/GaSb IMF interface. 23

2.2.1 Introduction. 23

2.2.2 Experimental processes. 25

2.2.3 Results and discussions. 26

2.2.4 Summary. 33

2.3 Defect analysis and measurement by TEM 34

2.3.1 Compressive IMF GaSb/GaAs interface. 35

2.3.2 Tensile IMF GaAs/GaSb interface 41

2.4 The application of IMF interfaces 43

References for chapter two 47

Chapter 3 Formation of Interfacial Misfit Dislocation Arrays for AlSb bulk on Si substrate 49

3.1 Issues of IMF growth mode on Si substrate 49

3.2 Anti-phase domains and boundaries. 50

3.3 Growth and characterization of AlSb on Si substrate 55

3.3.1 Preparation of Si substrate and growth. 55

3.3.2 AlSb on (100) Si. 56

3.3.3 AlSb on 5° miscut (100) Si. 62

3.4 Defect analysis and density measurement by TEM 70

3.5 Applications of AlSb/Si IMF 74

3.6 Summary 76

References for chapter three 77

Chapter 4 Interfacial misfit based GaSb QDs on GaAs substrate 79

4.1 Introduction. 79

4.2 Formation of interfacial misfit array based GaSb QDs. 81

4.3 Formation of Stranski-Krastanov GaSb QDs. 83

4.4 Optical properties of IMF QDs and SK QDs. 85

4.5 Summary. 90

References for chapter four 92

Chapter 5 Conclusions 93

LIST OF FIGURES

Figure 2.1: The ray diagram for a TEM in (a) the bright-field mode and (b) selected-area electron diffraction (SAED) mode.. 11

Figure 2.2: The schematic of STEM system. 13

Figure 2.3: Schematic of determining the Burgers vector for an edge-dislocation 15

Figure 2.4: Cross sectional TEM image of 100 nm of GaSb on GaAs. Part a) shows a highly periodic array of misfit dislocations at the interface between the GaSb epilayer and the GaAs substrate. Part b) shows its selected area electron diffraction (SAED) pattern. 16

Figure 2.5: (a) Cross sectional high resolution TEM (HRTEM) image of 100 nm of GaSb epilayer grown on GaAs substrate. (b) Schematic of determining Burger's vector and (c) Schematic of the atomic arrangement indicating the IMF interface.. 18

Figure 2.6: AFM images of the growth of GaSb on GaAs after (a) 3 ML deposition and (b) 9 ML deposition, showing formation of islands that are elongated along the [1-10] direction. 20

Figure 2.7: The growth of GaSb on GaAs after 9 ML deposition (a) Cross sectional TEM along [110], (b) Cross sectional TEM along [1-10], and (c) plan view HRSEM, showing formation of planar growth of islands that are elongated along the [1-10] direction. 21

Figure 2.8: HRSEM images of the etched GaSb surface after 60 s As_2 soak (a) plan-view, (b) side-view..... 26

Figure 2.9: 10 Å GaAs grown on GaSb surface, (a) AFM image, (b) Cross-sectional TEM image showing partial GaAs coalescence 28

Figure 2.10: (a) Cross-sectional TEM image of GaAs/GaSb interface featuring nano-voids, (b) HRTEM image of a void at the GaAs/GaSb interface 29

Figure 2.11: Cross-sectional TEM images of the tensile GaAs/GaSb interface, GaAs grown on GaSb after GaSb surface (a) 60 s, (b) 10 s, and (c) 0 s As_2 soak..... 31

Figure 2.12: (a) HRTEM image of the tensile GaAs/GaSb interface, featuring 90° IMF array. (b) Schematic of the atomic arrangement indicating the IMF interface. 32

Figure 2.13: Cross-sectional TEM images of GaSb/GaAs interface, (a) IMF growth mode, (b) non-IMF growth mode... 35

Figure 2.14: Plan-view TEM images of 54 ML GaSb on GaAs grown at 510 °C, [001] bright field image showing the misfit dislocations along both [110] and [1-10] directions, indicating IMF array at the compressive GaSb/GaAs interface 37

Figure 2.15: Plan-view TEM images of 54 ML GaSb grown on GaAs, a) (220) b) (2-20) images indicating IMF array at the compressive GaSb/GaAs interface 38

Figure 2.16: Plan-view TEM images of 5 μm GaSb grown on GaAs, (a) IMF growth mode with perfect surface, (b) IMF growth mode with few dislocations, (c) non-IMF growth mode... 40

Figure 2.17: Plan-view TEM images of the GaAs surface grown on GaSb after GaSb surface (a) 60 s, and (b) 0 s As_2 soak, indicating the defect density 41

Figure 2.18: Schematic of double-IMF VLED, illustrating an embedded GaSb active region between GaAs/AlGaAs layers... 44

Figure 2.19: RT, CW characteristics of the VLED showing (a) EL spectrum centered at 1600 nm, and (b) forward bias LIV characteristics. 45

Figure 2.20: RT, CW characteristics of the VLED showing the forward and reverse bias I-V characteristic curve. 46

Figure 3.1: Two sublattices in Si substrate 51

Figure 3.2: An anti-phase boundary (APB) in III-V materials 52

Figure 3.3: The formation of antiphase boundarys (APBs) in III-V materials on a (100) surface with steps 53

Figure 3.4: The antiphase boundary (APB) in AlSb on (100) Si substrate 53

Figure 3.5: Two types of double steps on a Si (100) surface 54

Figure 3.6: AFM images show surface morphology after (a) 3 ML, (b) 9 MLs (c) 18 ML and (d) 54 MLs of AlSb deposition on Si substrate. The inserts of (a) and (d) also show the RHEED patterns during the corresponding growth process 57

Figure 3.7: Figure 3.7: (a) Cross sectional TEM image of AlSb on Si, showing defect-free buffer layer. (b) HRTEM image of high quality GaSb grown on AlSb/Si, with periodic misfit dislocations along the AlSb/Si interface 58

Figure 3.8: TEM images show the structure of 100 nm GaSb / 10 nm AlSb / Si surface (a) low-resolution, (b) high-resolution, indicating the formation of lots of APDs and defects after AlSb deposition on (100) Si substrate 59

Figure 3.9: STEM images show the structure of 100 nm GaSb / 10 nm AlSb / Si surface (a) low-resolution, (b) high-resolution, indicating that there are no interdiffusion between the AlSb epilayer and (100) Si substrate 61

Figure 3.10: Cross-sectional TEM images of AlSb grown on 5° miscut Si (001) substrate under (a) low-resolution, (b) high-resolution conditions, and (c) highlighted section of figure (b), featuring the periodic IMF array 64

Figure 3.11: Series of schematics to eluciate atomic arrangement and resulting strain involved in AlSb on miscut Si. Part (a) shows the step geometry on a 5º miscut Si substrate. Part (b) shows a "ball and stick" schematic of Al, Sb and Si sublattices. Part (c) indicates sources of strain at the step edge due to the h_1, h_2 mismatch 65

Figure 3.12: Cross-sectional TEM images of AlSb grown on 3° miscut Si substrate under (a) low-resolution and (b) high-resolution conditions featuring lots of defects and APDs... 67

Figure 3.13: Schematic of a 90° misfit array array at AlSb/Si interface 69

Figure 3.14: AFM images of the 1 μm GaSb grown on AlSb on (a) Si (001) surface, (b) 5° miscut Si surface, indicating the use of misoriented substrates is essential for the suppression of antiphase domains..... 70

Figure 3.15: Plan-view TEM image of the GaSb surface grown on AlSb on 5° miscut Si surface, indicating one of APBs on the surface, with very low APD density 71

Figure 3.16: Plan-view TEM image of the GaSb surface grown on AlSb on 5° miscut Si surface, a) defect surface area, b) perfect surface area, indicating very low defect density 72

Figure 3.17: AFM image of 1μm GaSb grown on AlSb on 5° miscut Si surface..... 73

Figure 3.18: Schematic of monolithic VCSEL structure shows GaSb/AlSb QWs in half-wave cavity surrounded by AlGaSb/AlSb DBRs 74

Figure 3.19: RT-PP VCSEL lasing at 1.65 μm, (a) L-L curve indicating threshold intensity at pump power of 0.1 mJ/cm^2 per pulse, (b) Spectra at pump intensities – 0.4 × I_{th} , 1.0 × I_{th} and 1.1 × I_{th} 75

Figure 4.1: AFM image of GaSb IMF QDs on GaAs substrate after 3 ML deposition... 81

Figure 4.2: XTEM image of 3 ML GaSb IMF QDs on GaAs substrate. 82

Figure 4.3: Plan-view TEM image of 3 ML GaSb IMF QDs on GaAs substrate..... 82

Figure 4.4: AFM image of GaSb SK QDs on GaAs substrate after 3 ML deposition..... 83

Figure 4.5: XTEM image of GaSb SK QDs on GaAs substrate after 3 ML deposition .. 84

Figure 4.6: [001] bright field plan-view TEM image of 3 ML GaSb SK QDs on GaAs substrate. 84

Figure 4.7: RT PL spectra of single layer of GaSb QDs at different V/III ratios ranging from 1 to 6.5. The PL peak and FWHM of GaSb QDs at V/III ratios of 1, 2, 4, or 6.5 are 1.14 μm and 64 meV; 1.34 μm and 53 meV; 1.38 μm and 56 meV; and 1.39 μm and 53 meV, respectively 86

Figure 4.8: RT PL spectra of single layer of GaSb QDs with V/III ratio of 2 at a total coverage ranging from 2 to 6. The PL peak of GaSb QDs at a total coverage of 2, 3, 4, and 6 ML are 1.12 μm, 1.28 μm, 1.33 μm, and 1.35 μm, respectively..... 87

Figure 4.9: Cross sectional TEM images of 10 stacked GaSb QDs with V/III ratio of (a) 2, and (b) 6.5 at a total coverage 4 ML..... 88

Figure 4.10: RT PL spectra of 10 stacked GaSb QDs at different V/III ratios (2 and 6.5). The spacer thickness between each QD layer is 15 nm..... 89

Figure 4.11: Symmetric 004 x-ray diffraction pattern for ten stacked GaSb QDs at different V/III ratios (2 and 6.5). 90

LIST OF TABLES

Table 2.1: Defect density of different thickness of GaSb epilayers grown on GaAs at various growth temperatures. 34

Chapter 1

Overview of III-V materials on GaAs and Si technology

1.1 The issues for large mismatched III-Sb material growth

The Sb-bearing compounds offer a wide range of electronic bandgaps, bandgap offsets and electronic barriers along with extremely high electron mobility[1,2] and therefore enable a variety of extremely fast, low power electronic devices and infrared light sources.[3,4] Lattice-mismatched epitaxy of Sb-based materials on GaAs and Si substrates has attracted considerable attention due to the numerous advances in optoelectronic devices that can be enabled including monolithically integrated lasers, detectors, solar cells and transistors.[5] Due to high lattice mismatch between the epilayer and substrate, the material relieves strain energy through misfit dislocations and often threading dislocations,[6] which vertically propagate to active regions of devices. It leads to non-radiative recombination and damages device performance.[7]

To date, exploiting lattice-mismatched GaSb/GaAs and GaAs/GaSb heterojunctions is of considerable interest for III-Sb electronic and optoelectronic devices on GaAs substrates such as mid-wave infrared lasers, and transistors.[3,8] The ability to embed GaSb layers in a GaAs/AlGaAs could lead to the development of a new class of mid infrared vertical cavity lasers and the growth of GaSb on GaAs substrates would help realize detectors on transparent and semi-insulating GaAs substrates. The development of

mismatched growth techniques, such as metamorphic buffers, has helped in the growth of compressive GaSb/GaAs heterojunctions.[9] However, the tensile GaAs/GaSb interface leads to the usual threading dislocations and also material defects such as microcracks that are associated with tensile strain. If we can realize GaAs grown on GaSb with low defect density, it may be useful for embedded GaSb layers in a GaAs matrix.

Under compressive growth conditions, researchers have attempted to mitigate these detrimental effects by bending the vertically propagating defects along strained interfaces using compositionally graded-layers or selective area growth.[9,10] Another approach to developing low defect or defect-free bulk material is to design a lattice-mismatched interface in which strain energy is solely relieved by laterally-propagating (90°) misfit dislocations confined to the epi-substrate interface.[11,12] If the same interfacial misfit (IMF) dislocations can be applied to the tensile GaAs/GaSb heteoepitaxy, it could help realize high quality GaAs growth on GaSb.

Similarly, the heteoepitaxial growth of compound semiconductors on Si has received much attention. Most of these works are concentrated on the growth of GaAs on Si.[13,14] Since large-area, high-quality Si substrates are available, heteroepitaxy of compound semiconductors on Si is attractive. Meanwhile, it also affords the possibility of monolithic integration of compound semiconductor optical and electronic devices with complex Si integrated circuits. However, mismatch in lattice constant, thermal expansion coefficient and process temperature prevents the establishment of a stable and repeatable production process. Therefore, monolithic device characteristics have been marginal due

to micro-cracks and high dislocation density in the GaAs buffer.[15] As we know, the interfacial misfit (IMF) array based growth method can be applied to grow highly mismatched materials and yield low defect density of epilayer. Therefore, the application of IMF array on the monolithic integration of III-Vs with Si substrate using a special III-Sb nucleation layer will be one of tasks in this dissertation.

1.2 The concept of interfacial misfit array

The interfacial misfit (IMF) array based growth mode allows us to grow highly mismatched and low defect density epi-layer material. Under optimized growth conditions, a wide variety of materials can be realized the heteroepitaxy through IMF.

A critical thickness has to be achieved prior to the onset of misfit dislocations, in some materials systems such as GaSb on GaAs, where a two-dimensional (2D) array of misfit dislocations forms at the GaSb/GaAs interface.[11] This is a fundamentally different growth mode that results in high quality bulk material with very low defect density in which strain energy is solely relieved by laterally-propagating (90˚) misfit dislocations confined to the epi-substrate interface.[12]

However, the formation of an interfacial misfit array (IMF) does not proceed through the critical thickness way, but instead makes use of atomic arrangements on the surface of substrate to spontaneously relieve the high strain energy between the epi-layer

and substrate. When the growth conditions are not conducive to forming this atomic arrangement on the substrate, however, the growth then turns to a psedudomorphic growth process. The highly periodic nature of the IMF array, its long-range order and the fact that this arrangement can be picked up by in-situ measurements such as reflective high energy electron beam (RHEED) pattern indicate that the growth process may occur by self-assembly.

1.3 Objective for the work

The concept of IMF arrays is applied to highly lattice mismatched III-Sb epilayers grown monolithically on GaAs and Si substrates, and GaAs on GaSb substrate. According to theoretical calculations and material properties, we design special growth processes and optimize growth conditions to obtain high quality heteroepitaxial epi-layers through IMF growth mode.

The growth of III-Sb materials on GaAs and Si substrates and GaAs on GaSb substrate are characterized using a variety of tools such as – transmission electron microscopy (TEM), scanning transmission electron microscopy (STEM), atomic force microscopy (AFM), scanning electron microscopy (SEM), x-ray diffraction (XRD), and photoluminescence (PL).

References for chapter one:

[1] S. M. Sze, Semiconductor Devices, Wiley, New York, (2002).

[2] H. K. Choi, Long-Wavelength Infrared Semiconductor Lasers, Wiley, (2004).

[3] L. Shterengas, G.L. Belenky, A. Gourevitch, D. Donetsky, J.G. Kim, R.U. Martinelli, and D. Westerfeld, IEEE Photonics Technol. Lett. **16**, 2218 (2004).

[4] C. Mourad, D. Gianardi, and R. Kaspi, J. Appl. Phys. **88**, 5543 (2000).

[5] R.J. Malik, J.P. van der Ziel, B.F. Levine, C.G. Bethea, and J. Walker, J. Appl. Phys. **59**, 3909 (1986).

[6] J. W. Matthews and A. E. Blakeslee, J. Cryst. Growth **27**, 118 (1974).

[7] K-N. Tu, J.W. Mayer and L.C. Feldman, Electronic Thin Film Science, Macmillan (1992).

[8] M. Shur, GaAs devices and circuits, Plenum press, New York, (1986).

[9] Ganesh. Balakrishnan, Shenghong Huang, Tomas J. Rotter, Andreas Stintz, L.R. Dawson, K. J. Malloy, H. Xu, and D.L. Huffaker, Appl. Phys. Lett. **84**, 2058 (2004).

[10] X.Y. Sun, R. Bommena, D. Burckel, A. Frauenglass, M.N. Fairchild, S.R.J. Brueck, G.A. Garrett, M. Wraback, and S.D. Hersee, J. Appl. Phys. **95**, 1450 (2004).

[11] A. Yu Babkevich, R. A. Cowley, N. J. Mason, and A. Stunault, J. Phys. Condens. Matter **12**, 4747 (2000).

[12] A. Rocher, Solid State Phenomena **19/20**, 563 (1991).

[13] B. Y. Tsaur and G. M. Metze, Appl. Phys. Lett. **45**, 535 (1984).

[14] Z. Mi, P. Bhattacharya, J. Yang, and K. P. Pipe, Electron. Lett. **41**, 742 (2005).

[15] D. G. Deppe, N. Jr. Holonyak, K. C. Hsieh, D. W. Nam, and W. E. Plano, Appl. Phys. Lett. **52**, 1812 (1988).

Chapter 2

Self-Assembled Interfacial Misfit Dislocation Arrays between GaAs and GaSb

2.1 Formation of compressive GaSb/GaAs IMF interface

2.1.1 Introduction

The growth of large mismatched materials on GaAs, GaSb and Si has attracted considerable attention due to the advancements that they would provide for devices. Examples of such systems include the growth of GaAs on Si and growth of metamorphic buffers such as InGaAs, AlInAs and AlGaAsSb on GaAs and the growth of AlInSb metamorphic buffers on GaSb substrates.[1,2] The quality of growth of mismatched materials is governed by the degree of the mismatch and the thickness of the epi-layer. During the initial stages of growth, the mismatched epi-layer tetragonally distorts itself to fit on a smaller lattice. However, with the introduction of mismatch, the epilayer is limited to a critical thickness, beyond which the material relieves strain energy through misfit dislocations and often threading dislocations.[3] These threading dislocations are highly unfavourable to the devices. In particular, vertically propagating threading dislocations are highly detrimental to device performance and in materials with defect densities > $10^5/cm^2$, excessive carrier loss is caused through non-radiative recombination.[4] To overcome this problem, we propose the growth of mismatched materials that can relieve strain through an alternate mechanism – a periodic array of 90°

misfit dislocations at the epi-substrate interface.[5] We explore the growth of bulk layers of GaSb grown on GaAs substrates that relieve strain by the special method proposed above. While we have been able to demonstrate certain material systems that can effectively relieve strain through the generation of interfacial periodic 90° misfit dislocation array, the parameters of growth are highly critical to the formation of such arrays and it is only in a small window that the material nucleates as desired.

In these previous demonstrations, both 90 ° and 60 ° misfit dislocations were present.[6] While the predominant strain relief mechanism was believed to be the 90° misfits, the minority 60 ° misfits were shown to cause threading dislocations in the GaSb. However, it has been established that there exist 60° misfits as well in the material that result from the interaction of the {111} planes of the coalescing islands and also that these exist at the boundaries of the islands. The presence of these 60° misfits is highly detrimental to the fabrication of devices, due to the fact they can use the (111) plane as the glide plane to propagate threading dislocations. The source of the 60 ° misfits is still unclear but attributed to the following aspects: a) island coalescence, b) growth temperature, and c) the degree of the material mismatch. Firstly, the island coalescence process, in which the {111} planes of adjacent islands merge, has been shown to cause 60° misfits. It is obvious that we can find a strong correlation between island coalescence and the location of the 60 ° misfits. As for the growth temperature, researchers indicated that there is a strong factor in determining which type of misfit is produced, with GaSb grown at ~ 520 ºC favoring 90 ° misfits and 560 ºC favoring 60 ° misfits.[7,8] However, 560 °C may be too close to the melting temperature. Finally, the experimental results

have shown that the lattice mismatch has also been shown to be of critical importance in the formation of 90 ˚ misfits. Low strain systems (< 2 %) have resulted in 60 ˚ misfits, moderate strain (3 - 4 %) systems in mixed 90 ˚ and 60 ˚ misfits, and high strain (> 6 %) systems in pure 90 ˚ misfits.[9]

According to our research work, the formation of 90 ° rather than 60 ° misfits seems to require balancing strain energy with adatom migration and is therefore a function of lattice mismatch, Sb overpressure and growth temperature. And if indeed the nucleation could be planar then we could grow layers of GaSb with 90° misfit dislocations alone, and this would result in defect free epitaxial growth of GaSb on GaAs. Therefore, we try to achieve this by using lower growth temperature during the deposition of GaSb to reduce the surface mobility, by using a higher growth rate of GaSb so as to proceed directly to a planar nucleation and by reducing the As-Sb intermixing to provide for a uniform lattice mismatch at the interface.[5]

2.1.2 Experimental processes

The growth of the GaSb bulk on GaAs is done in a VG 80 MBE reactor. The valved crackers are used for the As and the Sb sources. Substrate temperature is measured with a pyrometer. Growth is initiated with the deoxidation of the GaAs substrate at 600˚C. This is followed by the reduction of the substrate temperature to 560˚C and the growth of 1000 Å of GaAs to obtain a smooth surface. The surface reconstruction is constantly monitored by RHEED pattern and at this point is noted to be an expected (2 x 4) pattern indicating an As-rich surface. After completion of the

homoepitaxy, the substrate temperature is brought down to 510˚C with a constant As overpressure. At this point we close the As valve and the GaAs surface starts losing the surface As. This is confirmed by RHEED pattern that switches to a (4 x 2) Ga-rich surface. Once the (4 x 2) reconstruction is confirmed, Sb is introduced and soaked by opening the Sb valved cracker. The RHEED pattern shows traces of a clear 1 x 3 pattern indicating that a thin film of GaSb has formed on the surface. After that, we start the growth of GaSb at a growth rate of 0.6 ML/sec. The choice of a fast growth rate is to prevent the formation of islands and nucleate a planar 2-dimensional material. The RHEED pattern is unclear for the first three monolayers (MLs) and then switches over to a very clean 1 x 3 pattern. We find that the films grown extremely thin such as 3 – 9 MLs appear to be planar from the RHEED pattern, however as they were cooled to room temperature (with Sb overpressure till 300˚C), there is a severe reorganization of the surface between 510 ˚C and 400˚C and ultimately the surface RHEED pattern clearly shows chevrons confirming the presence {111} planes from islands on the surface.

2.1.3 TEM characterization techniques

2.1.3.1 Introduction

Transmission electron microscopy (TEM) is perhaps the most powerful analytical tool available to material analysis. It has the ability to give us information about the microstructure, crystallography, and chemistry on a fine scale and sensitivity. This section presents a short review of the instrument, imaging modes and analytical procedures in conventional transmission electron microscopy.

For this work, TEM is performed on JOEL 2010 and JOEL 2010F operated at 200 kV using a thermionic lanthanum hexaboride (LaB_6) source. The JEOL 2010 is a high resolution TEM with a spatial resolution of 0.194 nm. This instrument has a high brightness electron source, digital image recording, a computer-controlled sample goniometer, and a geometrically optimized x-ray detector.

Figure 2.1 is the ray diagram for a TEM. Briefly, a TEM operates by exciting electrons from a source, where the electrons are focused and collimated along the optic axis of the microscope and passed through a thin specimen (normally less than 1 μm). The transmitted electrons are then used to form an image, diffraction pattern, or chemical spectrum of the specimen.

The imaging system of a TEM consists of at least three lenses, as shown in Figure 2.1, the objective lens, the intermediate lens and the projector lens. The objective lens is the electromagnetic lens that is responsible for focusing the electrons after they passed through the specimen. The intermediate lens can magnify the first intermediate image, which is formed just in front of this lens, or the first diffraction pattern, which is formed in the focal plane of the objective lens, by decreasing the excitation. The projector lens is used predominately to control the final magnification of the image or diffraction pattern on the viewing screen.

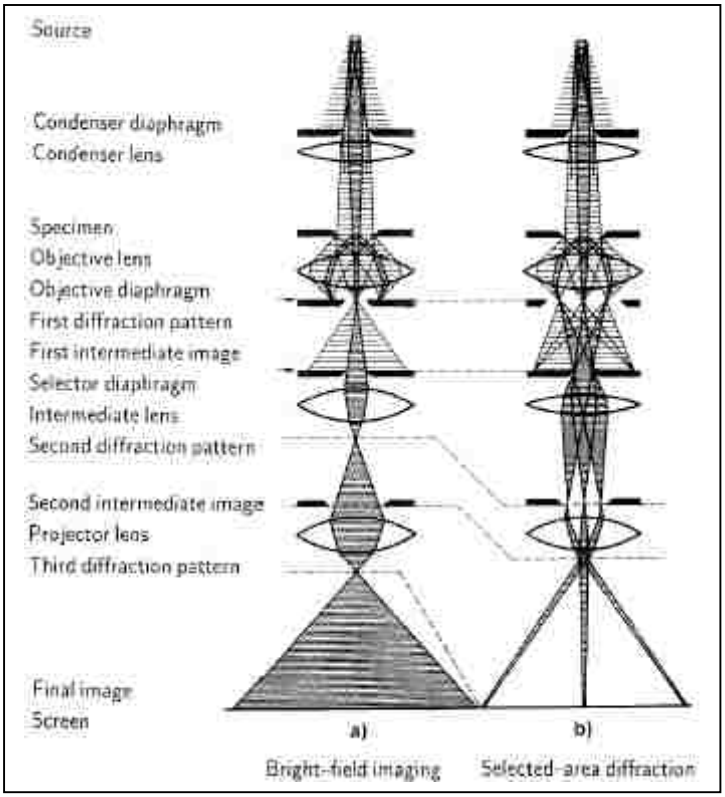

Figure 2.1: The ray diagram for a TEM in (a) the bright-field mode and (b) selected-area electron diffraction (SAED) mode.[10]

2.1.3.2 Imaging modes

The bright-field mode (BF) with a centered objective diaphragm is the typical TEM mode, as shown in Figure 2.1 (a), by selecting the primary beam and a cone of scattered electron. The dynamical theory of electron diffraction indicates that bright-field images will show the dependence of primary beam intensity on specimen thickness and tilt resulting in thickness fringes and bend contours.[11]

Dark-field (DF) images can be generated by tilting the illuminating beam so that the spot of the primary beam is intercepted by the objective diaphragm and only scattered

electrons pass through the diaphragm.[11] If we select Bragg reflections, the contrast of dislocations and other crystal defects can be improved.

2.1.3.3 Electron diffraction modes

Electron diffraction pattern can be used to extract additional information and obtain a better understanding of electron scattering in crystals. The first diffraction pattern in the focal plane of the objective lens can be imaged onto the screen either by exciting an additional diffraction lens or by reducing the strength of the intermediate lens. By inserting a selector diaphragm at the first image, the specimen area contributing to the diffraction pattern can be limited, i.e. selected area electron diffraction (SAED). Normally, a diffraction pattern consists of the primary beam of small aperture, the Bragg diffraction spots.

2.1.3.4 STEM modes

Unlike the conventional transmission mode of a TEM, where the whole imaged specimen area is illuminated simultaneously, the specimen is scanned in a raster point-to-point with a small electron probe in the scanning transmission mode.[10] The schematic of STEM system is shown in Figure 2.2.

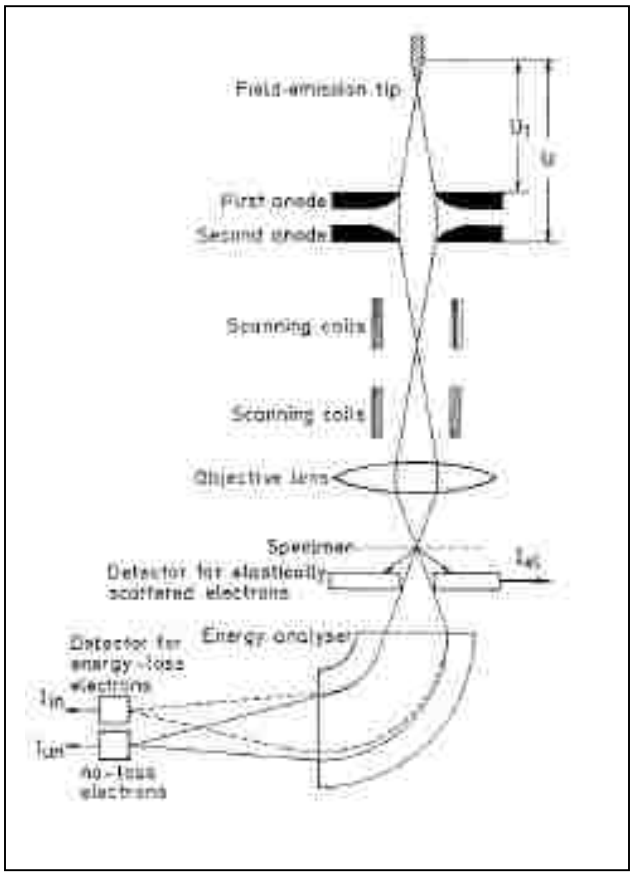

Figure 2.2: The schematic of STEM system. [10]

The virtual source of a field-emission gun is demagnified by an objective lens to an electron probe of about 0.1 – 0.2 nm.[10] A spectrometer is used to create the electron energy-loss spectroscopy (EELS) of the transmitted electrons. Simultaneously, we can also collect the signals related to unscattered, inelastically scattered and elastically scattered electrons.

By recording the ratio signal of elastically and inelastically scattetred electrons, the STEM can optimize the contrast for imaging single atoms.[11] Such a ratio signal can also be used to generated Z-ratio contrast image.

2.1.3.5 High-resolution TEM images

When the information about the lattice structure, i.e., the primary and the Bragg reflected beam, pass through the objective diaphragm and that the contrast is not destroyed by insufficient spatial and temporal coherence, the crystal lattice planes can be imaged and resolved.[12] The imaging of lattice planes only requires coherent superposition of the primary beam and a reflected beam in the image plane.

For the imaging of crystal structure, it is necessary to ensure that as many Bragg reflections as possible contribute to the image. The ideal image will be a projection of atomic rows, which appear as black dots when the irradiation is exactly parallel to a low-indexed zone axis.[10,13,14]

2.1.3.6 Burgers vectors

The Burgers vector of a dislocation is a crystal vector, specified by Miller indices, that quantifies the difference between the distorted lattice around the dislocation and the perfect lattice. Meanwhile, the Burgers vector denotes the direction and magnitude of the atomic displacement that occurs when a dislocation moves. There are two primary types of dislocations: edge dislocations and screw dislocations. Mixed dislocations are intermediate between these.

In a two-dimensional primitive square lattice, the Burgers vector of a dislocation can be determined as follows:

1) Draw a closed circuit that encloses the dislocation from lattice to lattice point, shown in Figure 2.3 (a);

2) Draw exactly the same chain of base vectors in a perfect reference lattice, shown in Figure 2.3 (b);

3) The special vector needed for closing the circuit in the reference crystal is by definition the Burgers vector ***b***. shown in Figure 2.3 (b).

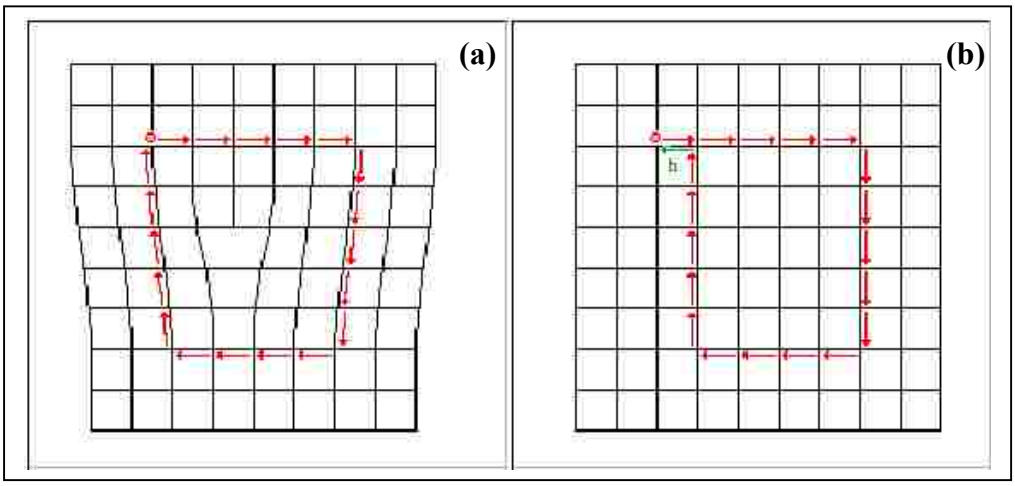

Figure 2.3: Schematic of determining the Burgers vector for an edge-dislocation.

2.1.3.7 Sample preparation

Transmission electron microscopy (TEM) specimens are prepared by mechanically polishing samples using diamond-lapping films ranged from 0.1 μm – 30 μm. The thickness of polished samples should be, usually, less than 10 μm. The samples were then ion-milled (Gatan model 600 dual ion mill) with Ar as the incident species at an angle of 10° – 12° to the sample surface until electron transparency. This process occurred at 4.0 - 4.5 kV voltage and ~ 1 mA of current. The ion-milled process of cross

sectional TEM (XTEM) samples occurred at both sides, while plan-view TEM images are ion-milled only from substrate side.

2.1.4 Results and discussions

The resulting bulk materials and misfit array have been analyzed carefully using low-resolution and high-resolution TEM images, shown in Figure 2.4. Figure 2.4 (a) shows a cross-sectional TEM (XTEM) image of a strain-relaxed, defect-free 100nm GaSb buffer grown on GaAs substrate and the GaSb/GaAs interface along the [1-10] direction.

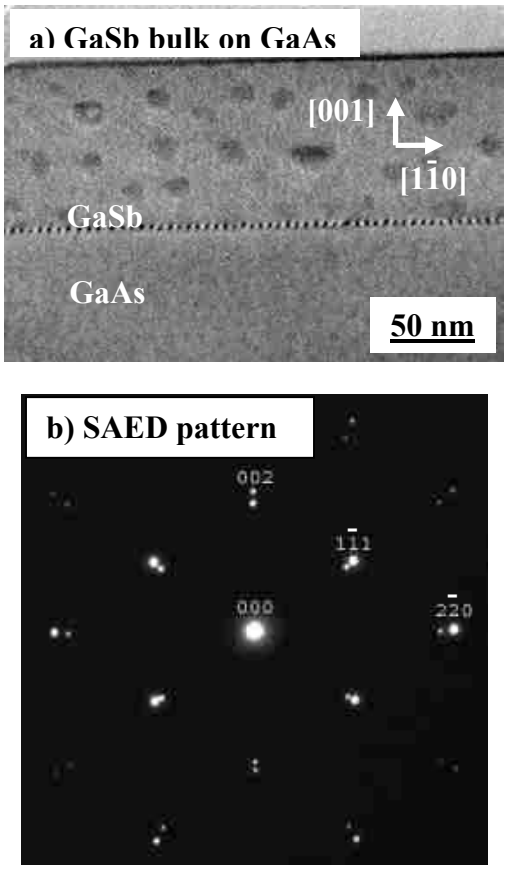

Figure 2.4: Cross sectional TEM image of 100 nm of GaSb on GaAs. Part a) shows a highly periodic array of misfit dislocations at the interface between the GaSb epilayer and the GaAs substrate. Part b) shows its selected area electron diffraction (SAED) pattern.

The misfits are arranged in highly periodic array. There are no misfit dislocations in any other part of the image except the GaSb/GaAs interface and there is a complete absence of any features that would suggest a growth mode involving islands. More specifically we do not see the presence of misfit dislocations in the material at any other location except for the interface that would be associated with the coalescence of large islands. This is further verified by the complete absence of threading dislocations in this section of the material. Selected area electron diffraction (SAED) pattern has been taken along the GaSb/GaAs interface, shown in Figure 2.4 (b), which indicates that the two sets of cubic diffraction spots are initially overlapped, and gradually separated with the increase of the plane indexes. The higher order spots are split into two spots, corresponding to each of the two materials. It reveals that GaSb epilayer has the same crystal growth orientation as that of GaAs layer, and the GaSb deposit is virtually fully relaxed in respect to the GaAs substrate.

Careful examination of the atomic lattice surrounding the interfacial misfits using cross-sectional HRTEM image, as shown in Figure 2.5 (a), can identify these misfits. Using the Burger's circuit theory around a misfit dislocation, shown in Figure 2.5(b), indicates that the Burger's vector, i.e., $\frac{a}{2}\left[1\bar{1}0\right]$, lies along the interface and identifies this misfit as 90° pure edge type. The misfit separation, measured to be 5.6 nm, corresponds to exactly 13 GaSb lattice sites grown on 14 GaAs lattice sites. The identical misfit arrays have been observed along both [110] and [1-10] directions, which shows that there is a 2D 90° pure edge dislocation array at the compressive GaSb/GaAs interface. The schematic Figure 2.5 (c) shows that the GaAs to GaSb ratio is precisely 14:13. It can be

verified with very simple arithmetic that the lattice space occupied by 14 atoms of GaAs along the [110] direction is about the same as that occupied by 13 atomic spaces of GaSb. This is shown as follows:

For GaAs, $(14 \times d_{110}) = 14 \times (5.65/1.414) = 55.94$ Å

For GaSb, $(13 \times d_{110}) = 13 \times (6.09/1.414) = 55.99$ Å

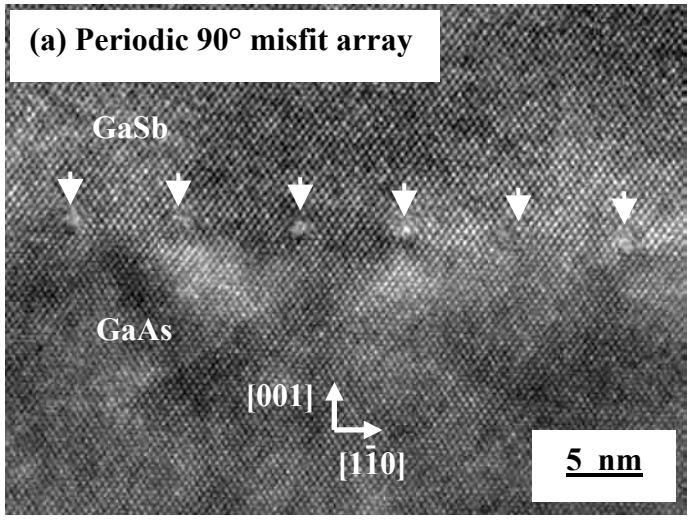

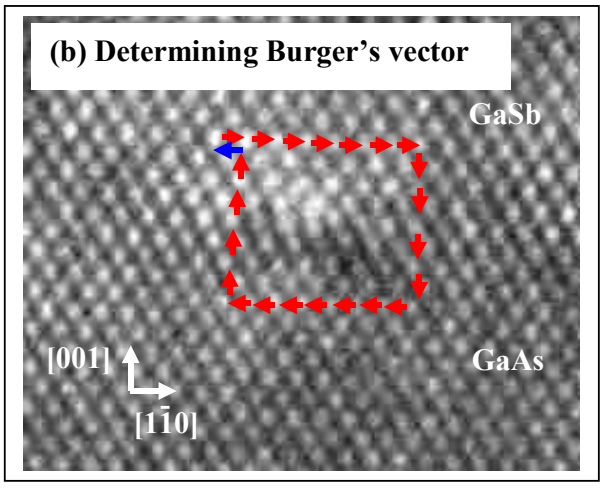

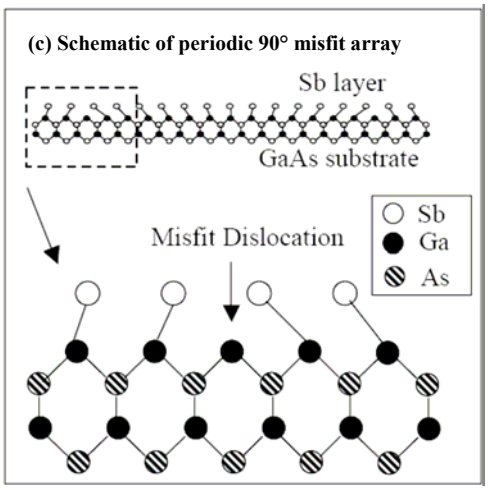

Figure 2.5: (a) Cross sectional high resolution TEM (HRTEM) image of 100 nm of GaSb epilayer grown on GaAs substrate, (b) Schematic of determining Burger's vector and (c) Schematic of the atomic arrangement indicating the IMF interface[15].

We have attempted further studies of the interface growth mode using AFM images and RHEED pattern. As noted above, the RHEED pattern transforms from a 4 x 2 to a 1 x 3 reconstruction within the first 3 MLs of GaSb deposition on GaAs as the Ga-terminated surface yields to the Sb-terminated surface. However, if the growth is terminated and the substrate temperature reduced after only a few monolayers, i.e. at 3 or 9 MLs, the 1 x 3 reconstruction transforms into a spotty RHEED pattern indicating an island ensemble forms. Figure 2.6 shows AFM images of the growth of GaSb on GaAs after (a) 3 ML deposition and (b) 9 ML deposition. As mentioned before, both these runs had planar RHEED signatures to begin with and during the cooling process proceeded to give a spotty RHEED pattern. There is a clear elongation of the islands along the (1-10) direction. The 3 ML deposition results in slightly elongated [1-10] islands that are 6 nm in height, 120 nm length, and 80 nm width with fairly uniform size distribution. The 9 ML deposition leads to larger highly elongated islands with a large variation in island size. Average dimensions are 10 nm in height, 450 nm length, and 120 nm width.

In order to verify if the formation of IMF occurs in both [110] and [1-10] directions, we analyze the interface features of the growth mode using cross-sectional TEM (XTEM) images and high-resolution scanning electron microscope (HRSEM) images. Figure 2.7 (a) and (b) show the cross-sectional TEM images after 9 ML GaSb deposition on GaAs surface, cleaved along the [110] and [1-10] directions, respectively. These images clearly show the presence of periodic interfacial misfit (IMF) dislocation array at the compressive GaSb/GaAs interfaces along both [110] and [1-10] directions. The dislocation separation is measured to be ~ 50-60 Å. 9 ML GaSb deposition leads to

larger elongation along [1-10] direction than [110] direction, which have the similar results as AFM images. The average heights are ~ 10 nm in both directions. No threading dislocations are observed in these particular islands or in numerous other islands. Defective islands are also visible on this surface and have no misfit dislocations at the interface. Therefore, it indicates the importance of the misfits in enabling this high quality growth mode.

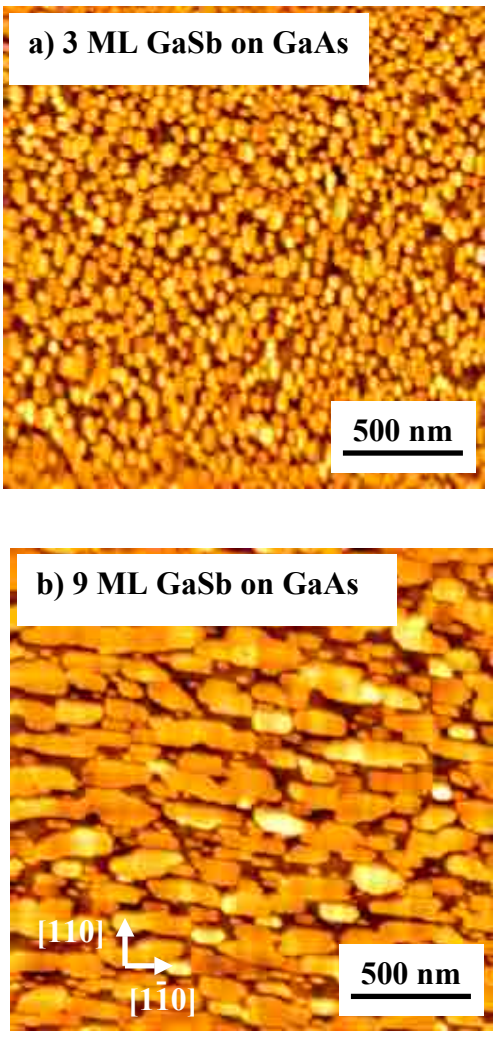

Figure 2.6: AFM images of the growth of GaSb on GaAs after (a) 3 ML deposition and (b) 9 ML deposition, showing formation of islands that are elongated along the [1-10] direction.

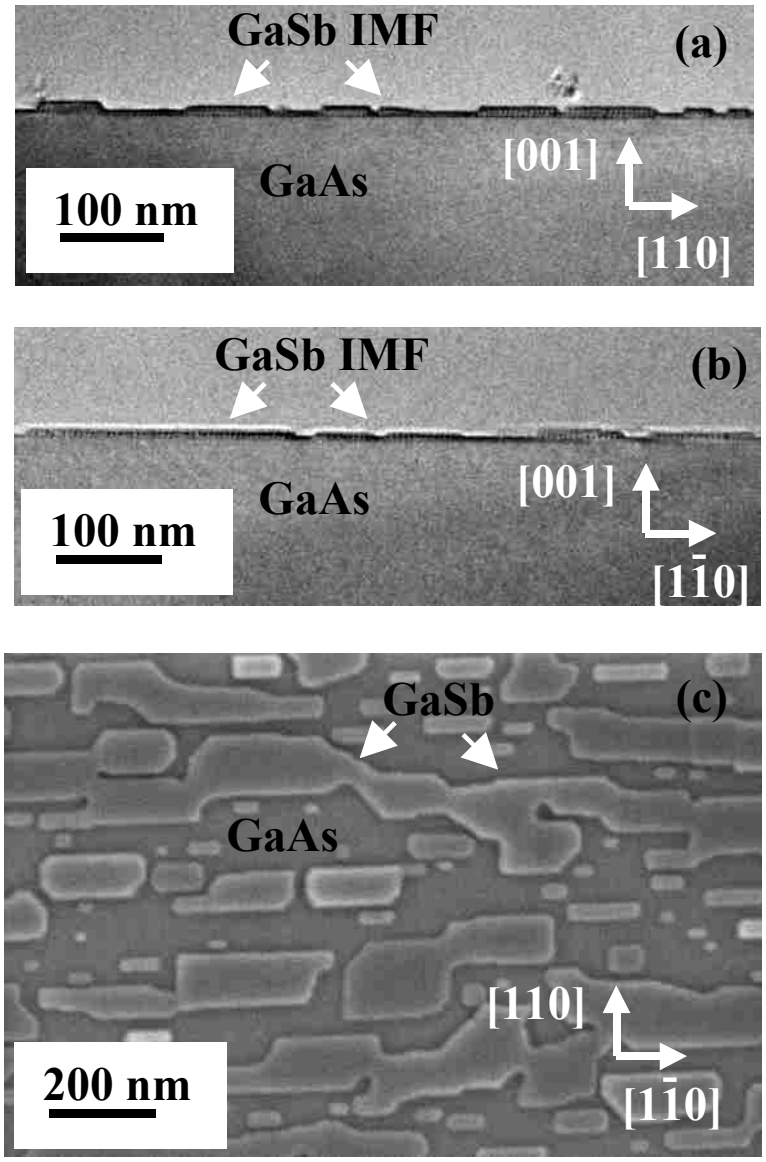

Figure 2.7: The growth of GaSb on GaAs after 9 ML deposition (a) Cross sectional TEM along [110], (b) Cross sectional TEM along [1-10], and (c) plan view HRSEM, showing formation of planar growth of islands that are elongated along the [1-10] direction.

Figure 2.7 (c) shows a plan-view SEM image of GaSb surface after 9 ML GaSb deposition on (100) GaAs surface. It also indicates that there is larger elongation along [1-10] direction than [110] direction. The plan-view SEM image shows that these GaSb islands have even merged over 1 μm in length. The image contrast of the merged GaSb is

exactly the same, which indicates the growth of GaSb epilayer exists the same crystal plan, i.e. planar growth.

2.1.5 Summary

In conclusion we have demonstrated that a periodic array of 90° misfit dislocations can be formed under specific growth parameters to fully relieve strain energy for growing bulk layers of threading dislocation free GaSb on GaAs. Furthermore, we see that under the growth conditions the growth of the GaSb is highly planar and proceeds directly to a 2D growth mode. We conclude that island formation that can be seen during the analysis of extremely thin films (~ 10 MLs) of GaSb on GaAs by AFM, SEM and TEM is due to surface reorganization during the sample cooling.

2.2 Formation of tensile GaAs/GaSb IMF interface

2.2.1 Introduction

Exploiting lattice-mismatched GaSb/GaAs and GaAs/GaSb heterojunctions are of considerable interest for III-Sb electronic and optoelectronic devices on a GaAs substrate such as mid-wave infrared lasers, detectors and transistors.[16,17,18] The ability to embed GaSb layers in an GaAs/AlGaAs could lead to the development of a new class of mid infrared vertical cavity lasers and the growth of GaSb on GaAs substrates would help realize detectors on transparent and semi-insulating GaAs substrates. The development of mismatched growth techniques such as metamorphic buffers have helped in the growth of GaSb/GaAs heterojunctions, with the dislocation densities reduced sufficiently to realize lasers, detectors and transistors.[1,19] The GaAs/GaSb interface, which is tensile with a 7.78% mismatch, leads to threading dislocations and also material defects such as microcracks that are associated with tensile strain. If we can realize GaAs grown on GaSb with low defect density, it may be useful for embedded GaSb layers in a GaAs matrix. The use of IMF dislocation array has been shown to reduce the threading dislocations in the growth of GaSb on GaAs significantly.[20,21] The use of the tensile IMF growth mode could help realize high quality GaAs growth on GaSb. In this section we investigate the tensile interfacial features in the growth of GaAs on GaSb.

The growth of GaSb on GaAs through an interfacial array of misfit dislocations is due to the antimony atoms forming a 2-dimensional reconstruction on the GaAs surface.[5] Before the Sb soak is initiated, the As valve is closed allowing As adatoms to be

desorbed leaving a Ga-rich surface. Once the GaSb growth begins, the RHEED pattern resembles a 1×3 indicating that a thin film of GaSb forms on the surface. The subsequent growth of GaSb on GaAs results in IMF array which is a completely relaxed growth mode with low defect density. This effect occurs due to the fact that the Sb atom forms one bond with the underlying Ga atoms but does not react with the GaAs substrate to displace the As atoms. This effect has been noted by Losurdo et. al.[22] where they document a positive enthalpy of reaction for the anion exchange reaction ($2GaAs + Sb_2 \rightarrow 2GaSb + As_2$, $\Delta H° = 47.6$ kJ/mol) and a reaction with an isoelectronic compound formation ($GaAs + Sb_2 \rightarrow GaSb + AsSb$, $\Delta H° = 13.7$ kJ/mol). However, no Sb soak before GaSb growth yield a spotty RHEED pattern with continued deposition that indicates a defective growth mode. It indicates that the Sb soak process is very important to form interfacial misfit array at the GaSb/GaAs interface.

When a similar reconstruction is tried with the growth of GaAs on GaSb, the As_2 specie reacts with the GaSb surface very aggressively due to a negative enthalpy of reaction for both the anion exchange reaction and the isoelectronic AsSb compound formation reaction ($GaSb + As_2 \rightarrow 2GaAs + Sb_2$, $\Delta H° = -47.6$ kJ/mol; $GaSb + As_2 \rightarrow GaAs + AsSb$, $\Delta H° = -33.9$ kJ/mol).[22,23] This makes it very difficult to establish a reconstructed As layer on the GaSb surface. The growth of GaAs on GaSb also results in the formation of interfacial features such as highly faceted nano-scaled pits.[24] Furthermore TEM analysis of these pits indicates that while some pits are formed during a pregrowth As soak of the GaSb surface, this etch results in a series of voids at the GaAs/GaSb interface. And the following deposition of GaAs nucleates on the unetched

GaSb surface and proceeds to coalesce over the etched voids. With the decreasing of the arsenic soak time prior to the growth of GaAs layer, the reaction between the As_2 specie and GaSb surface is suppressed, which leads to high quality GaAs epilayer. The purpose of this study is to quantify the interface quality with various soak times.

2.2.2 Experimental processes

The samples used in this interfacial analysis are grown on a V80H reactor with valved crackers for both the As and the Sb source. The crackers are operated at 900°C and 950°C respectively so that the molecular species from the sources are As_2 and Sb_2. The growth is initiated on a GaSb substrate with a thermal oxide desorption process. This is followed by a GaSb smoothing layer grown at 510 ºC at a growth rate of 0.5 μm/hr with an Ga/Sb flux ratio of 1:10. The RHEED pattern is used to verify a 1 x 3 pattern indicative of extremely smooth GaSb. At this point the growth is paused and excess Sb is allowed to desorb from the GaSb surface. The surface is then subjected to an As_2 overpressure with an approximate beam equivalent pressure of1 x 10^{-6} mTorr. This overpressure is maintained for 0 sec, 10 sec or 60 sec, respectively. Before the As growth is initiated, the Sb valve is closed allowing Sb atoms to desorb leaving a Ga-rich surface. This process, which is confirmed by RHEED indicating Ga-rich (4×2) pattern, reduces Sb/As intermixing. Following the soak, the GaAs growth is initiated without any changes in the growth temperature resulting in a smoothing of the surface with continued growth.

2.2.3 Results and discussions

Figure 2.8 shows the SEM images of the GaSb surface after 60 sec of exposure to the As overpressure ((a) plan-view, (b) side-view). The pits vary in both size and shape with average dimensions ~ 25 nm wide and 50 - 80 nm long and 10 - 70 nm deep, and a pit density of ~1 x $10^9/cm^2$. There appears to be no significant directionality to the pits. The side view (b) shows the image of the (110) cleaved facet with a 30 nm wide pit intercepted by the cleaving plane. While the resolution available using the HR-SEM is not sufficient to resolve the faceting in the pits, this study clearly establishes the pit formation as a result of the reaction of the As_2 with the GaSb substrate.

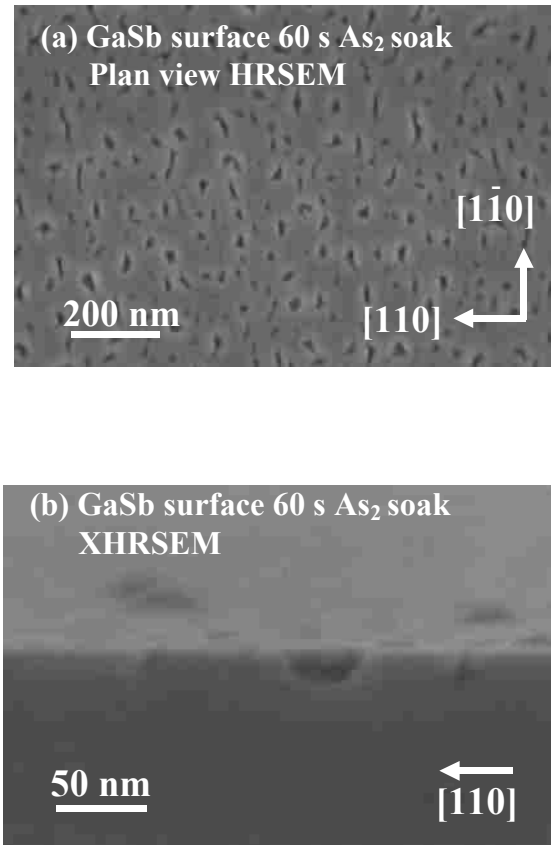

Figure 2.8: HRSEM images of the etched GaSb surface after 60 s As_2 soak (a) plan-view, (b) side-view.

Figures 2.9 shows TEM images that elucidate the evolution of the GaAs overgrowth on the etched GaSb surface. Figure 2.9 (a) shows the AFM image after 10 Å (~3 MLs) of GaAs deposition on a GaSb surface exposed to As_2 for 60 sec. The AFM image shows surface remnants of the etched pits as dark areas and indicates only partial GaAs coalescence over the pit after the 3 ML deposition. The image shows a pit density of 1 x $10^9/cm^2$, which is consistent with that observed in Fig. 2.8 (a) using HRSEM. Figure 2.9 (b) shows, a cross-section TEM image of the same sample. The GaAs nucleates on the unetched GaSb surface and then proceeds to coalesce over the pits forming encapsulated nano-scale voids at the interface. There is no indication from this image that any GaAs growth occurs inside the etch-pits.

Figure 2.10 shows a TEM analysis of a completely coalesced GaAs layer, 100 nm thick grown on GaSb. Figure 2.10 (a) shows the GaAs/GaSb interface featuring several nano-scaled voids. The voids have dimensions consistent with those observed in SEM analysis in Fig. 2.8 (a). This image shows the different shapes of the voids formed at the GaAs/GaSb interface. The smaller voids are v-shaped defined by two enclosing {111} planes on each side. The larger voids have a truncated v-shape enclosed by {111} planes on the sides and a {100} plane in the bottom. The formation of these shapes is attributed to an anisotropic etch rate along the (111) and the (100) directions. The image also shows a significant threading dislocation density in the GaAs layer. Figure 2.10 (b) shows a high-resolution image of one of the v-shaped triangular voids. The image indicates the presence of amorphous material in the interior of the void, which appears as a thick coating on the {111} planes and does not produce any TEM diffraction pattern. The

amorphous material could either be excess Sb as a result of the anion exchange reaction or the isoelectronic AsSb compound as a result of the alternate reaction.

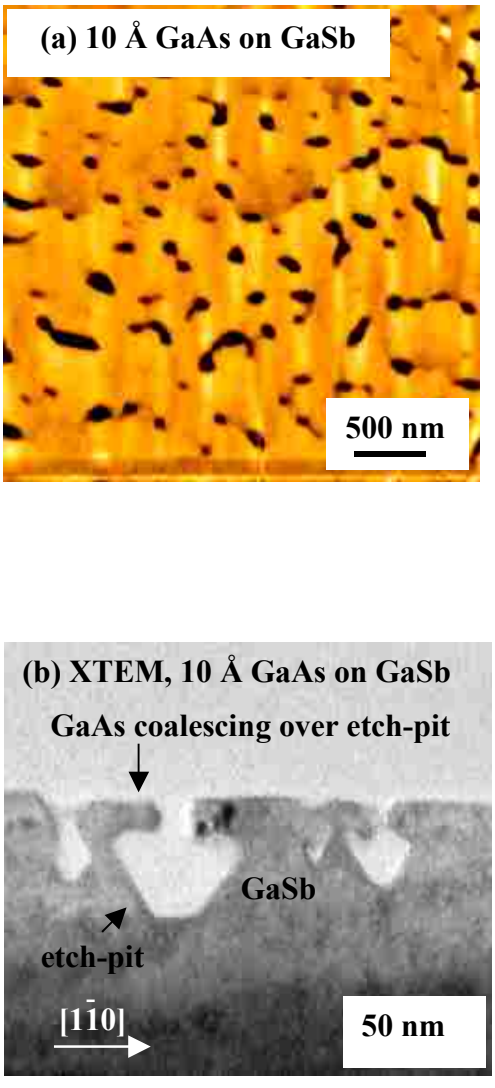

Figure 2.9: 10 Å GaAs grown on GaSb surface, (a) AFM image, (b) Cross-sectional TEM image showing partial GaAs coalescence.

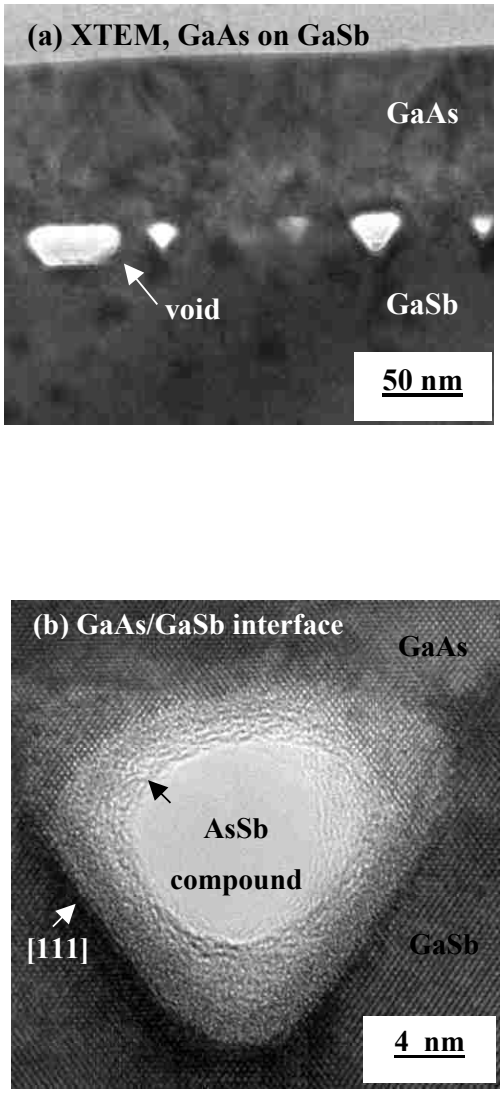

Figure 2.10: (a) Cross-sectional TEM image of GaAs/GaSb interface featuring nano-voids, (b) HRTEM image of a void at the GaAs/GaSb interface.

The resulting bulk materials and misfit array have been analyzed carefully using low-resolution and high-resolution TEM images. Figures 2.11 (a) (b) and (c) show the cross sectional TEM images for completely coalesced GaAs layers, 100 nm thick grown

on the GaSb surfaces under different As soak times (60 sec, 10 sec and 0 sec, respectively) prior to the growth of GaAs layer. At 60 s, as Figure 2.11 (a), the nano-scale etch-pits form at the GaAs/GaSb interface. These pits vary in both size and shape with average dimensions ~ 25 nm wide and 10 - 40 nm high. This image also shows a significant threading dislocation density in the GaAs epilayer ($>10^9/cm^2$). Using a 10 s As_2 soak time, the tensile GaAs/GaSb IMF array of moderate quality forms, shown in Figure 2.11 (b). Some etch-pits also appear along the GaAs/GaSb interface (not shown). The density of threading dislocations in GaAs epilayer decreases 2-3 orders of magnitude compared to Figure 2.11 (a), but remains high (10^7 /cm^2). If no As soak is used on the GaSb surface prior to the growth of GaAs layer, only tensile GaAs/GaSb IMF array forms at the interface, and produce good quality GaAs epilayer, as shown in Figure 2.11 (c). The limited cross-sectional area sampled by the TEM image indicates no threading dislocations, dark-line defects, or misfit dislocation except the tensile GaAs/GaSb interface. The bright spots in Figure 2.11 (c) correspond to misfit dislocation sites.[11] The misfits are arranged in a highly periodic array and localized at the tensile GaAs/GaSb interface. There is a strong indication that the interfacial misfit dislocation array can be realized if strong reaction between the As_2 and GaSb surface is suppressed. While the single As atomic layer seems to form on the Ga atomic layer by ambient As overpressure, it appears to lack long-range uniformity. This leads to a higher defect density than what can be realized in the compressive growth mode as indicated in plan-view TEM analysis shown below.

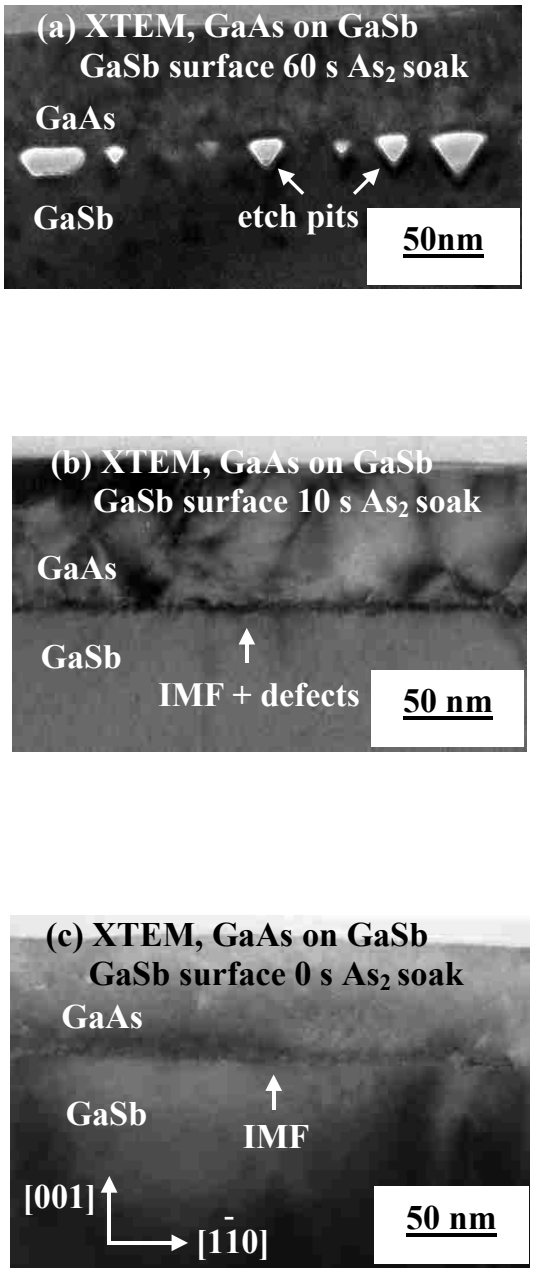

Figure 2.11: Cross-sectional TEM images of the tensile GaAs/GaSb interface, GaAs grown on GaSb after GaSb surface (a) 60 s, (b) 10 s, and (c) 0 s As_2 soak.

Careful examination of the atomic lattice surrounding the interfacial misfits using cross sectional HRTEM image, as shown in Figure 2.12 (a), can identify these misfits. Figure 2.12 (b) shows the atomic arrangement of the tensile GaAs/GaSb interface indicating the IMF.

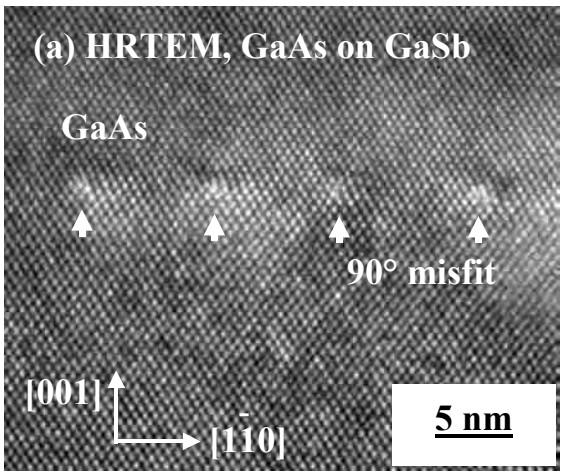

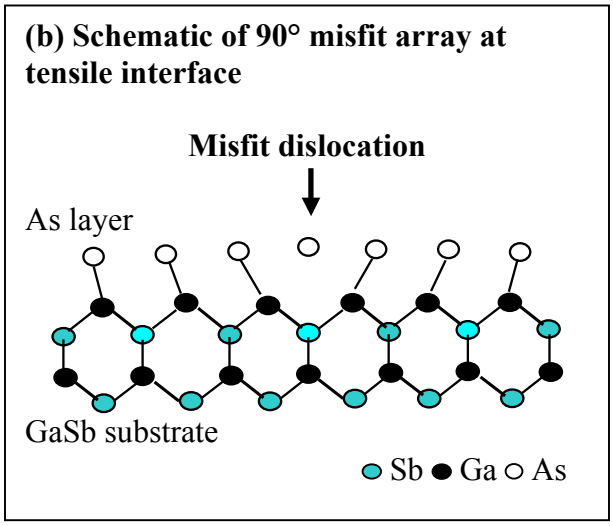

Figure 2.12: (a) HRTEM image of the tensile GaAs/GaSb interface, featuring 90° IMF array. (b) Schematic of the atomic arrangement indicating the IMF interface.

Using the Burger's circuit theory around a misfit dislocation shows that the Burger's vector, i.e., $\frac{a}{2}\left[1\bar{1}0\right]$, lies along the interface and identifies this misfit as 90° pure edge type. The misfit separation, measured to be 5.6 nm, corresponds to exactly 14 GaAs lattice sites grown on 13 GaSb lattice sites. The identical misfit arrays have been observed along both [110] and [1-10] directions, which shows that there is a 2D 90° pure edge dislocation array at the tensile GaAs/GaSb interface.

2.2.4 Summary

In conclusion, we have demonstrated that a periodic 90° misfit dislocation array can be formed under optimized growth conditions to relieve the high strain energy in the tensile lattice mismatch materials such as GaAs on GaSb once the reaction of the As_2 with GaSb surface is suppressed. The misfit separation, measured to be 5.6 nm, corresponds to exactly 14 GaAs lattice sites grown on 13 GaSb lattice sites. The IMF formation requires the As (001) atomic layer to self-assemble and bond to the underlying Ga (001) atomic layer. Bulk GaAs material with low dislocation density and strain-relieved properties is generated on GaSb layers by these growth conditions. Control of both tensile (GaAs on GaSb) and compressive (GaSb on GaAs) can lead to new devices based upon the novel integration schemes.

2.3 Defect analysis and measurement by TEM

In order to verify the quality of GaSb epilayer grown on GaAs, we first use the KOH etch-pit method to measure the density of dislocations. GaSb epilayers were grown on GaAs at different growth temperatures with GaSb thickness of 200nm, 1100nm and 3100nm, respectively, for each growth temperature. These wafers were then etched in 20% KOH solution for 10 minutes and roughly 100nm of the epi-layer was removed in each case. The measured results of etch-pit density are shown in Table 2.1, which clearly shows that the optimal growth temperature is ~510°C. At this temperature, the GaSb epilayer has the lowest etch-pit density compared to the GaSb epilayers grown at other growth temperatures.

Table 2.1: Defect density of different thickness of GaSb epilayers grown on GaAs at various growth temperatures.

GaSb thickness / Growth Temperature	100 nm	1000 nm	3000 nm
	(/cm^2)	(/cm^2)	(/cm^2)
480 °C	5×10^9	2×10^9	2×10^9
510 °C	8.5×10^5	7.4×10^5	5×10^5
540 °C	9×10^7	3×10^7	2.8×10^7

2.3.1 Compressive IMF GaSb/GaAs interface

As we pointed out in section 2.1, the growth parameters are very critical to the formation of IMF arrays and it is only in a small window that the material nucleates as desired. It is very important for the formation of 90° rather than 60 ° misfits to require balancing strain energy with adatom migration, thus the growth process has related to lattice mismatch, Sb overpressure and growth temperature. Under optimized conditions, the ideal compressive GaSb/GaAs IMF array can be formed, as shown in Figure 2.13 (a). We do not see the presence of misfit dislocations in the GaSb bulk layer at any other location except the interface. Obviously, there are no threading dislocations propagating to the epilayers along the growth direction.

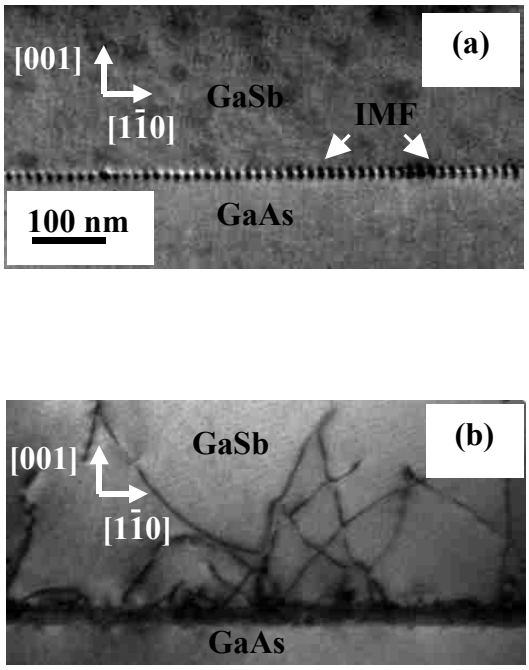

Figure 2.13: Cross-sectional TEM images of GaSb/GaAs interface, (a) IMF growth mode, (b) non-IMF growth mode.

We grow the same epi-structure at the same temperature, however, no Sb soak before GaSb growth with continued deposition yields a defective growth mode. The large mismatch between GaSb and GaAs is relieved by lots of misfit dislocations and threading dislocations, shown in Figure 2.13 (b). Thus, a non-IMF epilayer instead of an IMF epilayer forms at the compressive GaSb/GaAs interface. This non-IMF growth structure indicates that the Sb soak process is very important to form an interfacial misfit array at the compressive GaSb/GaAs interface.

Cross sectional TEM images have shown that IMF array do exist in the GaSb/GaAs interface. However, we know that IMFs only appear at either [110] or [1-10] direction, respectively. In order to directly demonstrate the formation of IMF at the interface, observing plan-view TEM images is only way available. We grew very thin (54 ML) GaSb bulk layer on GaAs substrate under optimized conditions so that it is convenient to be analyzed by TEM. Figure 2.14 shows a [001] bright field plan-view TEM image of 54 ML GaSb on GaAs grown at 510 °C where one can observe the misfit dislocations along both (110) and (1-10) simultaneously. It indicates that the IMF array exists obviously at the compressive GaSb/GaAs interface. If the misfit dislocation array consists of purely edge dislocations, the network is elastically stable since the dislocations have no tendency to attract or to repel each other.[6] Therefore, it is expected that there should be no threading dislocations in the bulk layer once the interface exists only a perfect 90° dislocation net. To further analyze the IMF array and measure the misfit separation, we take plan-view TEM images along diffraction vectors both $\boldsymbol{g}$(220) and $\boldsymbol{g}$(2-20) at the same sample.

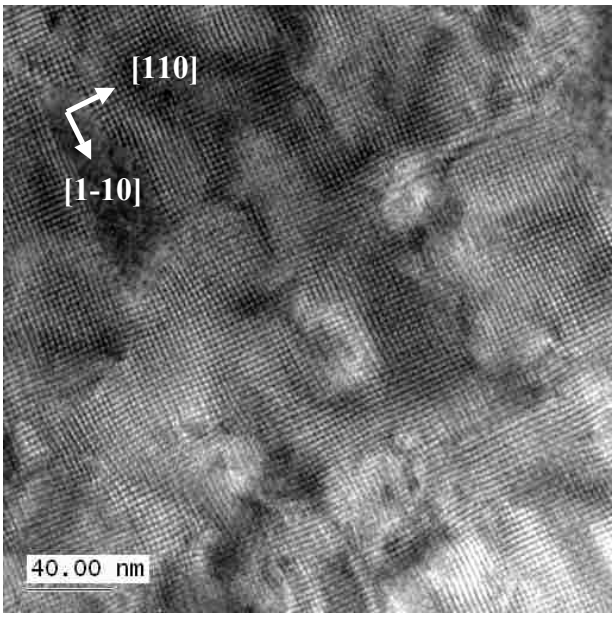

Figure 2.14: Plan-view TEM images of 54 ML GaSb on GaAs grown at 510 °C, [001] bright field image showing the misfit dislocations along both [110] and [1-10] directions, indicating IMF array at the compressive GaSb/GaAs interface.

Figure 2.15 (a) and (b) show (220) and (2-20) plan-view TEM image of the same sample shown in Figure 2.14, respectively. It reveals an array of Moiré fringes, which indicates that the IMF array consists mainly of 90° misfit dislocations at the compressive GaSb/GaAs interface along both [110] and [1-10] directions, which agrees with the results of cross-sectional TEM images, shown in Figure 2.7.Since the Moiré pattern can be used to locate and give information on dislocations which are present in one material.[11] When a 60° misfit dislocation segment "cut" through the [110] 90° misfit dislocation array, it can cause them to shift by half a period. Furthermore, the 60°

dislocations can easily glide on the close packed {111} planes to form threading segments in the GaSb bulk epilayer. As reported by Zhu and Carter,[25] this type of shift results from the interaction with a 60° dislocation. From plan-view TEM images of Figure 2.15, obviously, there are no half-period-shift of 90° dislocations at both directions.

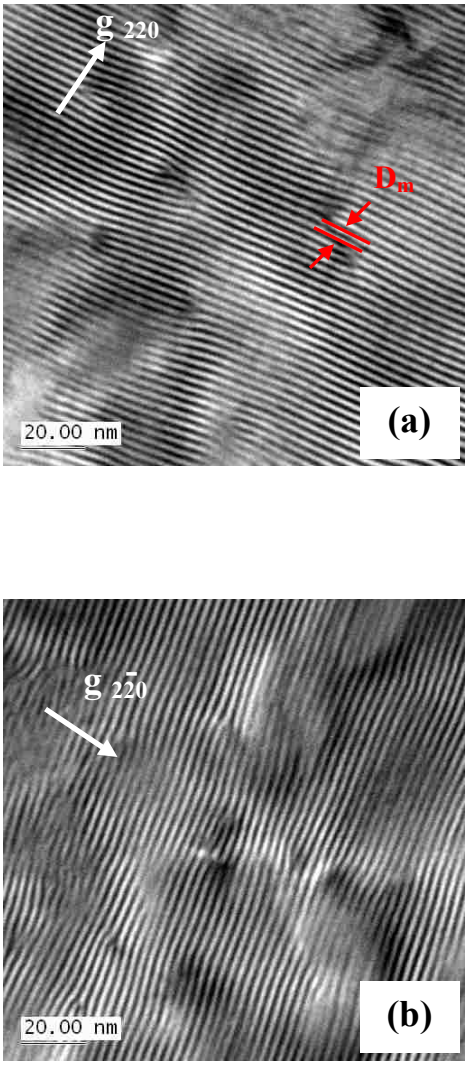

Figure 2.15: Plan-view TEM images of 54 ML GaSb grown on GaAs, a) (220) b) (2-20) images indicating IMF array at the compressive GaSb/GaAs interface.

The theoretical parallel Moiré fringes spacing for an epitaxial system, D_m, is given by the general equation:[11]

$$D_m = \frac{dd_1}{d_1 - d}$$

where d and d_1 are the interplanar spacings of parallel sets of planes in the substrate and the epilayer, respectively.

Assuming the lattice constant of GaSb a_{GaSb} = 6.096 Å, and the lattice constant of GaAs a_{GaAs} = 5.653 Å, the Moiré fringes spacing D_m for diffraction vector $\boldsymbol{g}$ = {220} reflections is 2.75 nm. While the measured value of ~ 2.83 nm is good agreement with the theoretical spacing, which indicates that the GaSb epilayer is almost fully relaxed.

Figure 2.16 shows the bright field plan-view TEM images of 5 μm GaSb grown on GaAs by IMF and non-IMF growth modes. Figure 2.16 (a) shows the center surface area with no defects. Figure 2.16 (b) features visible defects at the surface. This image, captured from an edge region where growth conditions are perhaps not optimum. Based on scanning different areas of the center of the wafer we estimate our defect density to be ~ 5.4 $\times 10^5$ defects/cm^2, which has similar results as Table 2.1. However, the dislocation density for the non-IMF growth sample with same epi-structure, shown in Figure 2.16 (c), is up to 4.8 $\times$ 10^9 /cm^2. It demonstrates absolutely that the IMF array can reduce greatly the propagation of threading dislocation to the epilayer, and thus improving the quality of bulk materials.

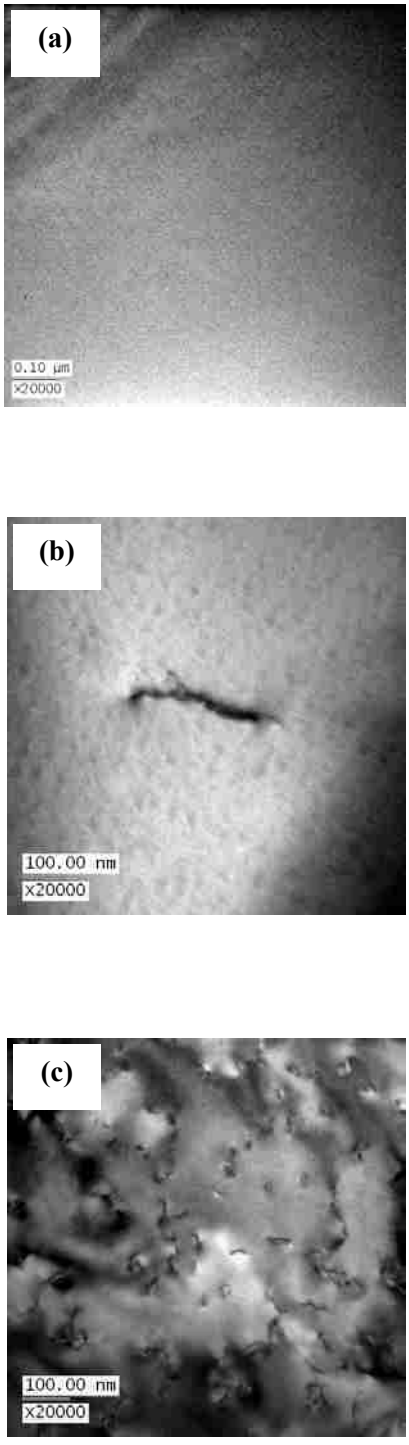

Figure 2.16: Plan-view TEM images of 5 µm GaSb grown on GaAs, (a) IMF growth mode with perfect surface, (b) IMF growth mode with few dislocations, (c) non-IMF growth mode.

2.3.2 Tensile IMF GaAs/GaSb interface

Figure 2.17 shows plan-view TEM images of the GaAs surface after GaSb surface (a) 60 s, (b) 0 s As_2 soak, respectively, prior to the growth of GaAs epilayer. These images indicate threading dislocations that appear as dark, squiggly lines on the shiny GaAs surface and enable the density of threading dislocations to be calculated. The 60 sec As_2 soak condition yields a threading dislocation density ~ 1×10^9 defects/cm^2. With no As_2 soak, the density of threading dislocation reduces ~ 3×10^6 defects/cm^2. This result is consistent with those observed in Figure 2.11 with cross sectional TEM analysis.

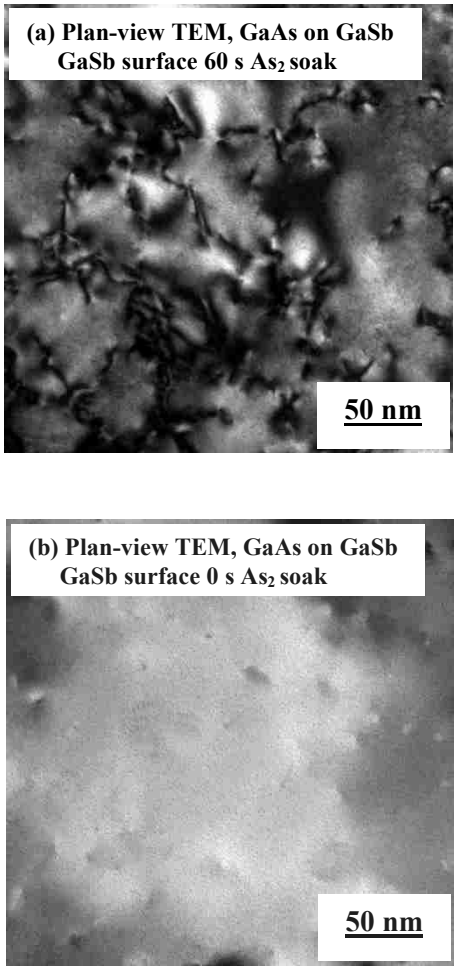

Figure 2.17: Plan-view TEM images of the GaAs surface grown on GaSb after GaSb surface (a) 60 s, and (b) 0 s As_2 soak, indicating the defect density. [26]

Compared to the formation of compressive IMF array, the tensile IMF array seems to produce more misfit dislocations. As what pointed out at previous sections, the Sb atoms have good surface mobility, thus, the single Sb atomic layer can easily form on the Ga atomic layer. While the single As atomic layer seems to form on the Ga atomic layer by ambient As overpressure, it appears to lack long-range uniformity. It is the reason why the tensile IMF array has higher density of misfit dislocation than that of compressive IMF array as indicated in plan-view TEM analysis.

However, to realize high performance electronic devices using the tensile IMF, the defect density of the GaAs on GaSb needs to be reduced $<10^5/cm^2$. To achieve the higher quality GaAs on GaSb, a non-reactive atom can be used either as a surfactant or catalyst. A thin buffer of AlSb, with greater bond strength compared to GaSb, may also reduce the As/surface reactivity enabling long-range uniform IMF formation.

2.4 The application of IMF interfaces

We have developed a hybrid, monolithic growth method to the mid-wave infrared (MWIR) emitters to apply both III-Sb bandgap for MWIR access and the advanced device design and processing advantages of the GaAs matrix in a monolithic vertical-cavity structure. We apply a 2-D array of 90˚ IMF, which produces strain-free, low-defect Sb-bearing bulk layers on GaAs. The large strain energy due to lattice mismatch is relieved immediately at the GaSb/GaAs interface. Meanwhile, we have also extended the IMF growth mode to tensile conditions that allows high quality bulk GaAs to be formed on GaSb. The ability to realize IMF arrays at both compressive and tensile interfaces, along with the buffer-free quality of the growth mode, allows a GaSb active layer to be monolithically embedded in a GaAs matrix.

The vertical cavity light emitting diode (VLED) incorporates a GaSb active region embedded within GaAs/AlGaAs DBR layers using both a compressive and tensile IMF array interfaces. Figures 2.18 illustrate the schematic of two interfacial misfits array in the VLED device grown by MBE method. It includes a 6.5 period GaAs/$Al_{0.92}Ga_{0.08}As$ bottom n-type DBR, five 100 Å GaSb QW separated by unintentionally doped $Al_{0.3}Ga_{0.7}Sb$ barriers and $Al_{0.3}Ga_{0.7}Sb$ n-type and p-type cladding layers, and a 1.5 period GaAs/$Al_{0.92}Ga_{0.08}As$ top p-type DBR. The electronic band structure surrounding both compressive and tensile interfacial misfit array has been modeled and analyzed, which indicates the IMF array presents a barrier to carrier flow at the interface due to Fermi level pinning.[27]

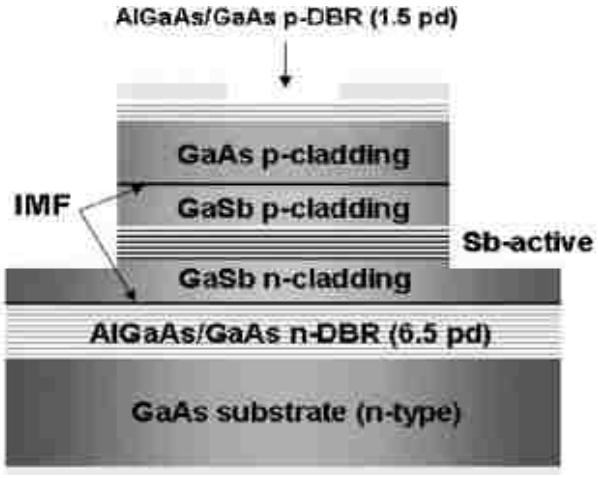

Figure 2.18: Schematic of double-IMF VLED, illustrating an embedded GaSb active region between GaAs/AlGaAs layers. [27]

Figure 2.19 shows room temperature (RT) continuous-wave (CW) electroluminescence (EL) and light-current-voltage (LIV) VLED characteristics. The RT EL spectrum of Figure 2.19 (a) shows a center wavelength of 1600 nm as expected from the GaSb QWs and spectral full-width at half-maximum (FWHM) of 78 meV at a current density of 100 mA/cm^2. The LIV VLED characteristics, as shown in Figure 2.19 (b), indicate a maximum output power, I=3.5 μW and an external efficiency, η_{ex}=0.007 %. Since this device has not current confinement, the geometry introduces a compulsory 15 times loss in external efficiency. We expect marked efficiency improvement (>10%) once current confinement is provided and doping/contact design is revised.

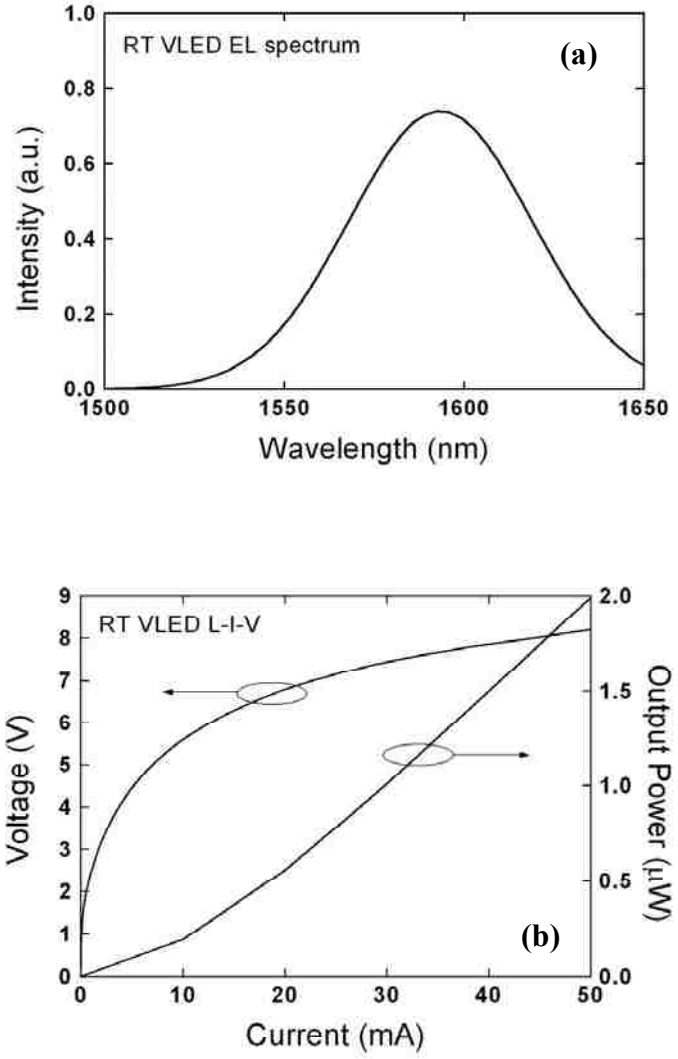

Figure 2.19: RT, CW characteristics of the VLED showing (a) EL spectrum centered at 1600 nm, and (b) forward bias LIV characteristics.

Figure 2.20 shows forward and reverse bias I-V characteristics. The reverse bias characteristics demonstrate low reverse bias leakage current densities of 0.01 A/cm^2 at -4 V, 0.1 A/cm^2 at -6 V and 2 A/cm^2 at –10 V, respectively, indicative of low defect density in the material. The non-optimized forward bias characteristics show a turn-on voltage of

~ 3 V and a differential resistance of ~ 30 Ω at 8 V. The rather high voltage is due in part to a large p-type specific contact resistance of $1x10^{-5}$ Ω-cm^2 caused by unoptimized doping and partially due to a ~1 V drop per IMF. The voltage drop associated with the IMF is confirmed in a controlled study that compares diodes without an IMF, with one IMF and two IMFs. This additional voltage drop at the IMF interface is caused by spikes in the bandstructure resulting from Fermi level pinning by the IMF-related dangling bonds.

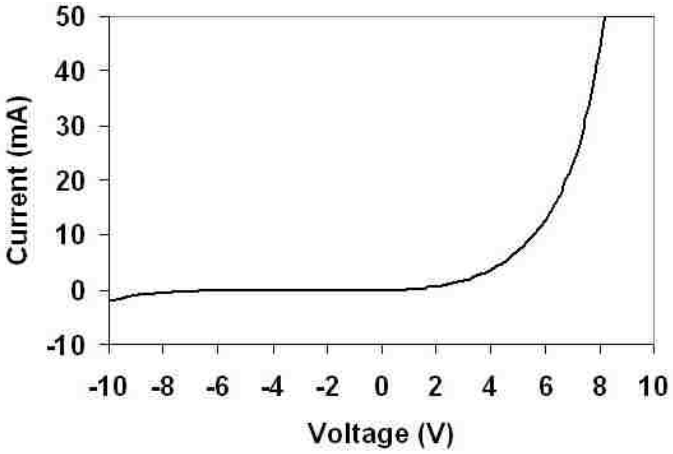

Figure 2.20: RT, CW characteristics of the VLED showing the forward and reverse bias I-V characteristic curve.

In summary, a hybrid, yet monolithic GaSb QW-based VCSEL that utilizes GaAs/AlAs DBRs for the resonant cavity has the potential to overcome many of the material difficulties in extending VCSEL operation into MWIR. The monolithic and bufferless IMF growth technique demonstrated in the VLED may be a precursor to realizing such a device once the challenges of current confinement and IMF barriers can be solved.

References for chapter two:

[1] Y.-C.Xin, L.G. Vaughn, L.R. Dawson, A. Stintz, Y. Lin, L.F. Lester and D.L. Huffaker, J. Appl. Phys. **94**, 2133 (2003).

[2] E.A. Pease, L.R. Dawson, L.G. Vaughn, P. Rotella, and L.F. Lester, J. Appl. Phys. **93**, 3177 (2003).

[3] J. W. Matthews and A. E. Blakeslee, J. Cryst. Growth **27**, 118 (1974).

[4] K-N. Tu, J.W. Mayer and L.C. Feldman, Electronic Thin Film Science, Macmillan (1992).

[5] S. H. Huang, G. Balakrishnan, A. Khoshakhlagh, A. Jallipalli, L.R. Dawson, and D.L. Huffaker, Appl. Phys. Lett. **88**, 131911 (2006).

[6] W. Qian, M. Skowronski M, R. Kaspi, M.D. Graef and V. P. Dravid, J. Appl. Phys. **81,** 7268 (1997).

[7] J. -H. Kim, T. -Y. Seong, N. J. Mason, and P. J. Walker, J. Electron. Mater. **27**, 466 (1998).

[8] W. Qian, M. Skowronski, and R. Kaspi, J. Electrochem. Soc. **144,**1430 (1997).

[9] R.E. Mallard, P.R. Wilshaw, N.J. Mason, P.J. Walker and G.R. Booker, Microsc. Semiconduct. Materi. 331 (1989).

[10] Ludwig Reimer, Transmission electron microscopy, Springer, (1997).

[11] D. B. Williams and C. Barry Carter, Transmission Electron Microscopy, Kluwer Academic/Plenum, New York, 1996.

[12] J. C. H. Spence, High-resolution electron microscopy, Oxford science publications, (2003).

[13] L. W. Hobbs, K. H. Westmacott, and D. B. Williams, Materials problem solving with the transmission electron microscope, MRS symposia proceedings, Vol.62, Materials Research Society, Pittsburgh, Pennsylvania, (1986).

[14] W. Krakow, D. A. Smith, and L. W. Hobbs, Electron microscopy of materials, MRS symposia proceedings, Vol. 31, North-Holland, (1984).

[15] A. Jallipalli, G. Balakrishnan, S. H. Huang, A. Khoshakhlagh, L. R. Dawson and D. L. Huffaker, accepted by J. Cryst. Growth, Dec. 2006.

[16] L. Shterengas, G. L. Belenky, A. Gourevitch, D. Donetsky, J. G. Kim, R. U. Martinelli, and D. Westerfeld, IEEE Photonics Technol. Lett. **16**, 2218 (2004).

[17] C. Mourad, D. Gianardi, and R. Kaspi, J. Appl. Phys. **88**, 5543 (2000).

[18] S. M. Sze, Semiconductor Devices, Wiley, New York, (2002).

[19] Ganesh Balakrishnan, Shenghong Huang, Tomas J. Rotter, Andreas Stintz, L.R. Dawson, K. J. Malloy, H. Xu and D.L. Huffaker, Appl. Phys. Lett., **84**, 2058, (2004).

[20] A. Rocher, Solid State Phenom. **19**, 563 (1991).

[21] A. Y. Babkevich, R. A. Cowley, N. J. Mason, and A. Stunault, J. Phys.: Condens. Matter. **12**, 4747 (2000).

[22] M. Losurdo, P. Capezzuto, G. Bruno, A. S. Brown, T. Brown, and G. May, J. Appl. Phys. **100**, 013531 (2006).

[23] Qianghua Xie, J. E. Van Nostrand, J. L. Brown, and C. E. Stutz, J. Appl. Phys. **86**, 329 (1999).

[24] S. H. Huang, G. Balakrishnan, M. Mehta, L.R. Dawson, D.L. Huffaker, and P. Li, submitted to J. Appl. Phys. Feb. 2007.

[25] J. G. Zhu and C. B. Carter, Phil. Mag. A **62**, 319 (1990).

[26] S. H. Huang, G. Balakrishnan, M. Mehta, A. Khoshakhlagh, L.R. Dawson, D.L. Huffaker, and P. Li, Appl. Phys. Lett., **90**, 161902, (2007).

[27] M. Mehta, G. Balakrishnan, S. H. Huang, L.R. Dawson, and D.L. Huffaker, Appl. Phys. Lett. **89**, 211110 (2006).

Chapter 3

Formation of Interfacial Misfit Dislocation Arrays for AlSb bulk on Si substrate

3.1 Issues of IMF growth mode on Si substrate

The monolithic growth of III-V materials on Si offers several desirable features such as efficient use of the integrating platform and reduced processing complexity. For over two decades, significant research and development efforts have focused on monolithic approach through a variety of methods.[1-9] The monolithic approach utilizing GaAs/AlGaAs has led to room-temperature edge-emitting laser and even vertical cavity lasers (VCSELs) on Si (100).[2,3] However, mismatch in lattice constant, thermal expansion coefficient and process temperature prevents the establishment of a stable and repeatable production process. Therefore, monolithic device characteristics have been marginal due to micro-cracks and high dislocation density in the GaAs buffer.[4] Recently, some of the prominent results are using SiGe metamorphic buffers,[5,6] and using GaAs metamorphic buffers on Si[7] that achieve dislocation bending through InAs quantum dot based strain fields.[8] Although these results are very encouraging, these devices suffer from reliability issues related to the growth on metamorphic buffers, GaAs/Si thermal mismatch, and high dislocation density in the GaAs buffer.[9,10,11] Meanwhile, there may be some industry application issues in which the thick buffer may be incompatible with the design for actual chip dimension and the manufacturing.

As shown, the IMF array based growth method can be applied to grow highly mismatched materials and yield an epilayer with low defect density.[12,13] In this chapter, we will focus the application of IMF array on the monolithic integration of III-Vs with Si substrate using a special AlSb nucleation layer. Use of AlSb circumvents these mismatch issues since thermal expansion coefficients are well matched ($\alpha_{Si} = 2.05 \times 10^{-6}$ / K, $\alpha_{AlSb} = 2.55 \times 10^{-6}$ / K) [14], the growth temperature is low and the material system spontaneously produce period 90º misfit array for strain relief. This growth mode is rather different from that of GaAs grown on Si, which mainly forms 60° dislocations and results in lots of threading dislocations propagating vertically into the material. The growth of AlSb on Si was first explored in the mid-1980s by Van der Ziel and co-workers. Most of the studies of AlSb on Si reported have been limited to X-ray diffraction studies and basic PL characterization.[15,16] Thus, the growth mechanisms of the highly mismatched epitaxy have not been identified. In this chapter we investigate the interfacial features and the mechanism of formation of IMF array in the growth of AlSb grown on Si (001) substrate.

3.2 Anti-phase domains and boundaries [17,18]

Besides the above material issues, a key element for the growth of group III-V materials on Si is the preparation of a surface that prevents antiphase domains (APD). Antiphase domains are commonly observed in the growth of compound semiconductors on elemental semiconductors. The problem is due to the fact that both the diamond cubic (Si) and zincblende (eg. AlSb) structures are composed of two interpenetrating face-

centered cubic (FCC) sublattices. The two sublattices differ from each other only in the spatial orientation of the four tetrahedral bonds that connect each atom to its four nearest neighbors, which are on the other sub-lattice.

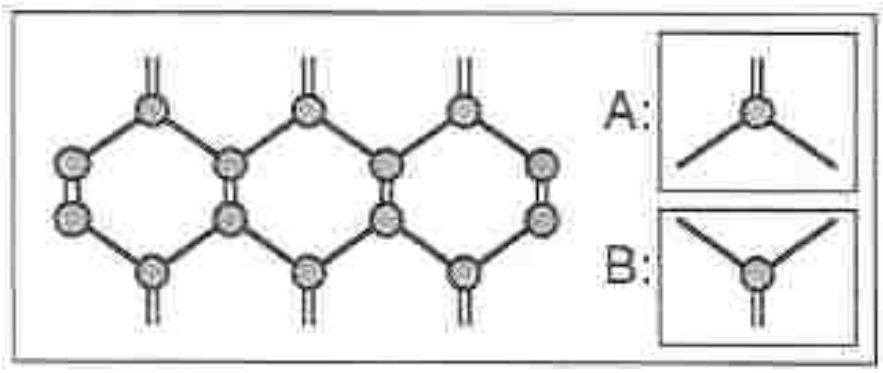

Figure 3.1: Two sublattices in Si substrate [17]

As shown in Figure 3.1, the atoms with bond orientations indicated as "A" and "B" belong to sublattices "A" and "B", which are occupied by the same atomic species. There is no any distinction between the sublattices. In the zinc-blende structure in which such as AlSb crystallize, one of the sublattices is occupied by the group III elements (Al), and the other by the group V elements (Sb). In a crystal without anti-phase disorder, the sublattice arrangement is the same throughout the whole crystal. However, if this arrangement changes somewhere inside the crystal, the interface between the domains with opposing sublattice arrangement forms a two-dimensional structural defect called anti phase boundary (APB) and the domains themselves are called anti-phase domains (APD),[18] shown in Figure 3.2.

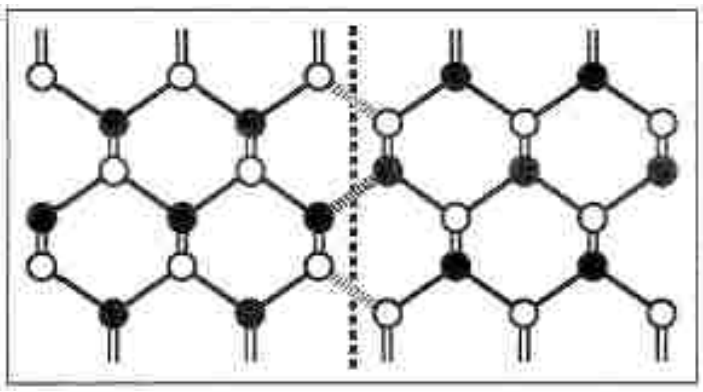

Figure 3.2: An anti-phase boundary (APB) in III-V materials. [17]

As we know, the (100) plane contains only one of the two FCC sublattices. But the real (100) surface contains steps, and if these steps are an odd number of atomic layers in height, then the surface is composed of atoms from both sublattices. Thus, when III-V materials are grown on such a Si surface, the problem of APBs and APDs will exist. Especially, the problem is further accentuated by lack of Si homoepitaxy, which results in rougher surfaces. The extensive domain formation is observed in the growth of all III-Vs materials (polar) on Si substrate (non-polar). For example, the polar AlSb material is grown on the non-polar silicon substrates. When growth of AlSb is initiated on the Si substrate, there are regions where aluminum and other regions where antimony nucleate first. When the regions coalesce, this difference in nucleation process results in Al-to-Al and Sb-to-Sb bonds. The Al-to-Al and Sb-to-Sb provide an excess positive and excess negative charge, respectively. These regions, termed anti-phase domains (APDs), continue from the growth front into the active regions of the device. This effect is shown in Figure 3.3. However, high quality compound semiconductor layers are prevented by the presence of the interfaces between the APDs.

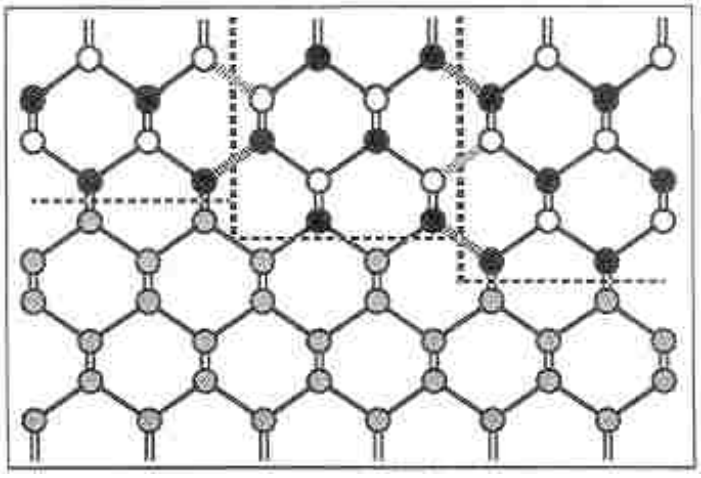

Figure 3.3: The formation of antiphase boundarys (APBs) in III-V materials on a (100) surface with steps. [17]

For the typical Si (100) wafer, the most common step height is one atomic layer and then the growth of III-V materials such as GaP or GaAs, on (100) Si or Ge substrates usually exhibits lots of APBs. Figure 3.4 shows a high resolution AFM image of AlSb grown on (100) Si substrate. This image clearly indicates that the APD defects exist on the surface of the epilayer.

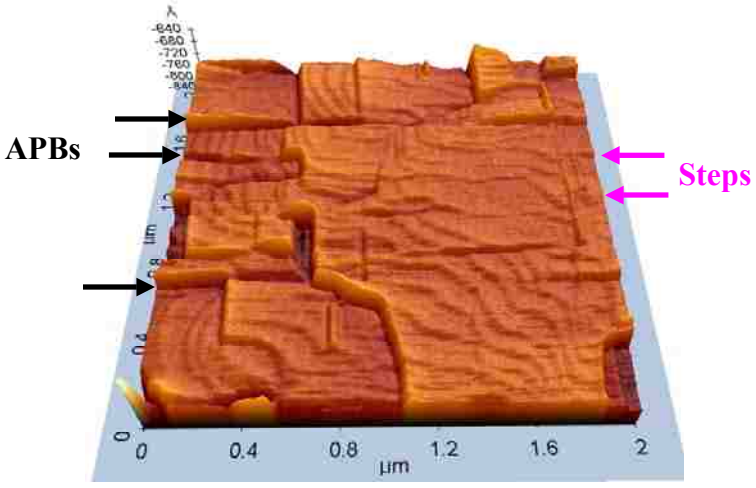

Figure 3.4: The APBs in AlSb on (100) Si substrate

When the steps on a Si(100) surface happen to be an even number of atomic layers in height, the two sublattices on the III-V material side are in registry again, thus APDs will not appear. Therefore, in order to realize the growth of free APDs, it is very important that all steps should be two atoms in height. So far, there are at least three methods towards the essentially complete suppression of APDs. Firstly, high temperature annealing greatly can improve the initial surface condition problem for APD free growth. Sakamoto and Hashiguchi[19] indicated that odd atomic layer steps have disappeared and atoms on the corresponding terraces have diffused on the surface to leave only even atomic layer steps. Secondly, switching to a different crystallographic orientation, such as (211), will lead to the absence of APDs.[20] Finally, one involves enforcing a perfect doubling of the height of essentially all surface steps. Figure 3.5 shows that there are two types of double steps on Si (100) surface. In the presence of double-height steps the surface layers on all terraces belong to the same Si sublattice, thus there must be a preference for one of the two Si sublattices over the other.

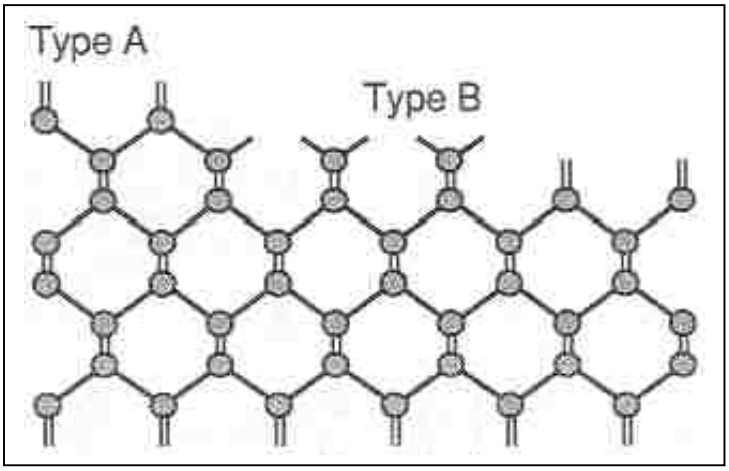

Figure 3.5: Two types of double steps on a Si (100) surface [17]

3.3 Growth and characterization of AlSb on Si substrate

3.3.1 Preparation of Si substrate and growth

The samples used in this interfacial analysis are grown on a V80H molecular beam epitaxy reactor. Prior to growth, the Si substrate surface is hydrogen-passivated by immersing the wafer in an HF solution bath. The HF solution is usually diluted to 1:10. Due to the reaction between surface SiO_2 and diluted HF solution, a clean Si surface with the dangling bonds passivated by hydrogen atoms is left behind. Heating the substrate to 500 °C in vacuum removes the loosely bonded hydrogen. A thermal cycle at 800 °C ensures the removal of the oxide remnants. The removal of the hydrogen is verified by RHEED pattern, which shows a 2 x 2 surface reconstruction.

The substrate temperature is reduced and stabilized at 510 °C followed by ~ 25 s Al soak and then 15 s soak in an Sb overpressure. Following the soak, the AlSb growth is initiated without any changes in the growth temperature resulting in a smoothing of the surface with continued growth.

The RHEED pattern proceeds through two distinct phases during the initial growth. The deposition of AlSb on Si results in an interconnected chevron pattern. Meanwhile, a 3 x 3 pattern is superimposed on this pattern. This implies that the initial growth of AlSb results in the formation of islands with {111} facets and truncated on top of (100) plane. After deposition of ~15 nm AlSb, the RHEED pattern becomes a pure 3 x 3 pattern, which indicates the start of a planar growth mode.

3.3.2 AlSb on (100) Si

For the growth of AlSb on Si substrate, we first analyze the initial growth process. Figure 3.6 shows that atomic force microscope (AFM) after 3 ML, 9 ML, 18 ML, and 54 ML of AlSb deposition, respectively. At 3 MLs of AlSb deposition, the QD density is 10^{11} /cm^2 with dot height and diameter of 1-3 nm and 20 nm, respectively. Continued deposition of 9 ML AlSb, shown in Figure 3.6 (b), causes the individual islands to coalesce but remain crystallographic. At 18 MLs, shown in Figure 3.6 (c), indicates a crystallographic preference of the coalescence along the [110] direction. Figure 3.6 (d) shows continued coalescence towards planar growth with 54 MLs of AlSb deposition on Si surface.

In addition, the insets show the corresponding RHEED patterns at each stage of the nucleation layer growth. At 3 MLs AlSb deposition, the RHEED pattern is spotty with overlaid chevrons characteristic of the QD growth, as shown in the insert of Figure 3.6 (a). After 54 ML deposition, the spotty/chevron character has transformed to a 3 x 1 pattern, indicating the initial of a planar growth, shown in the insert of Figure 3.6 (d).

The resulting bulk material has been carefully analyzed by low-resolution and high-resolution cross-sectional TEM (XTEM) images. Figure 3.7 (a) shows the XTEM image of AlSb (0.5 μm) grown on Si, indicating very low defect density. Figure 3.7 (b) shows the HETEM image of the strain-relaxed, defect-free GaSb (10 nm) on an AlSb

buffer (5 nm) nucleated on Si and the AlSb/Si interface. The misfits are arranged in a highly periodic array and localized at the AlSb/Si interface. The limited cross-sectional area sampled by the TEM image indicates no threading dislocations, dark-line defects, or misfit dislocation.

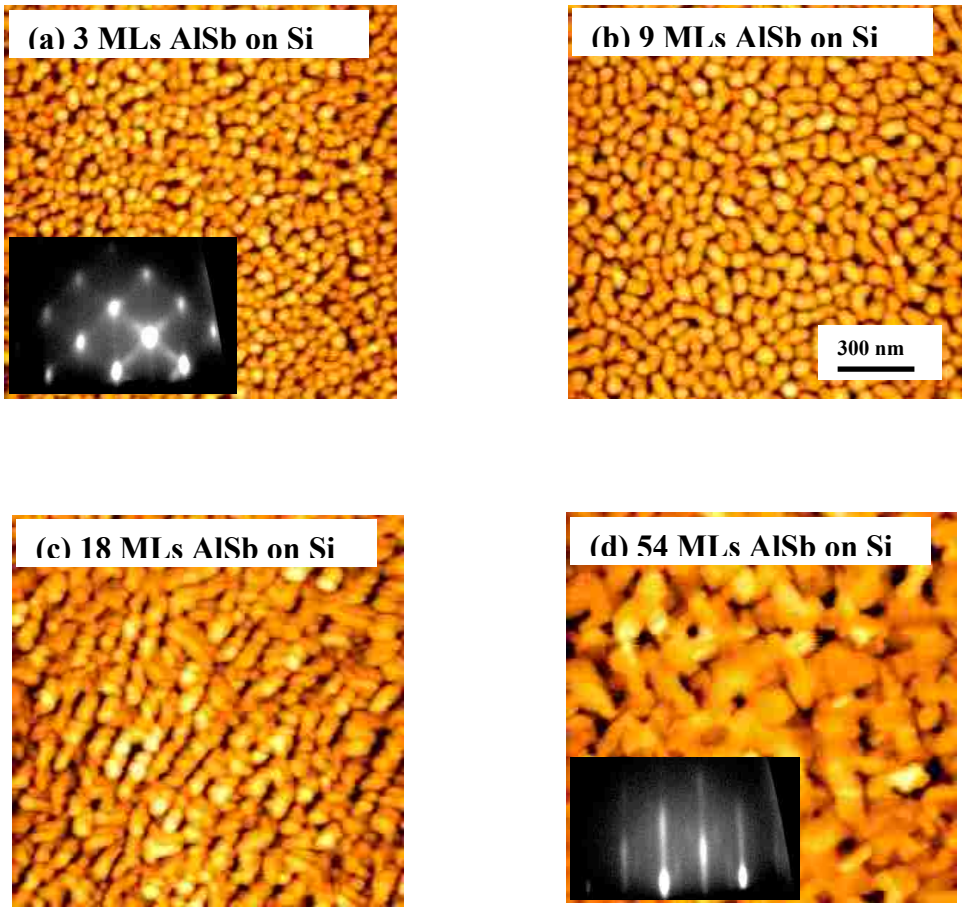

Figure 3.6: AFM images show surface morphology after (a) 3 ML, (b) 9 MLs (c) 18 ML and (d) 54 MLs of AlSb deposition on Si substrate. The inserts of (a) and (d) also show the RHEED patterns during the corresponding growth process.

Careful examination of the atomic lattice surrounding the misfits using cross sectional HRTEM image, as in Figure 3.7 (b), allows the identification of these misfits. Using the Burger's circuit theory around one misfit dislocation indicates that the Burger's

vector lies along the interface and this misfit as 90° pure edge type. The misfit separation, measured to be ~3.46 nm, corresponds to exactly 8 AlSb lattice sites and 9 Si lattice sites.

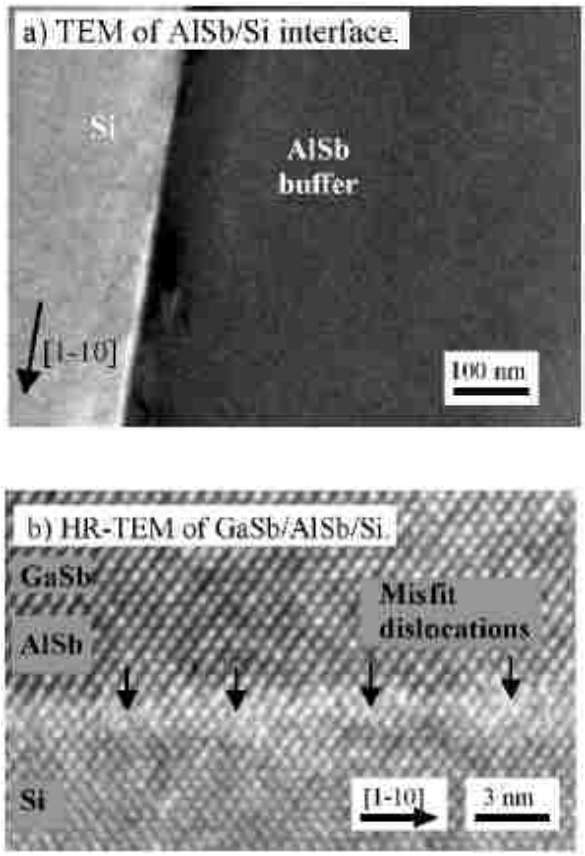

Figure 3.7: (a) Cross sectional TEM image of AlSb on Si, showing defect-free buffer layer. (b) HRTEM image of high quality GaSb grown on AlSb/Si, with periodic misfit dislocations along the AlSb/Si interface.

We further verify the quality of the epilayer and the nucleation layer of AlSb. Figures 3.8 (a), and (b) show the cross sectional TEM (XTEM) images of a bulk GaSb layers (100 nm) grown on AlSb (10 nm) on Si substrate. These XTEM images indicate that there are lots of APDs propagating vertically. HRTEM analysis indicates that the types of dislocations at the AlSb/Si interface include isolated 60° dislocations, pairs of

60° dislocations, and 90° dislocations. Therefore, the presence of APDs remains a critical problem.

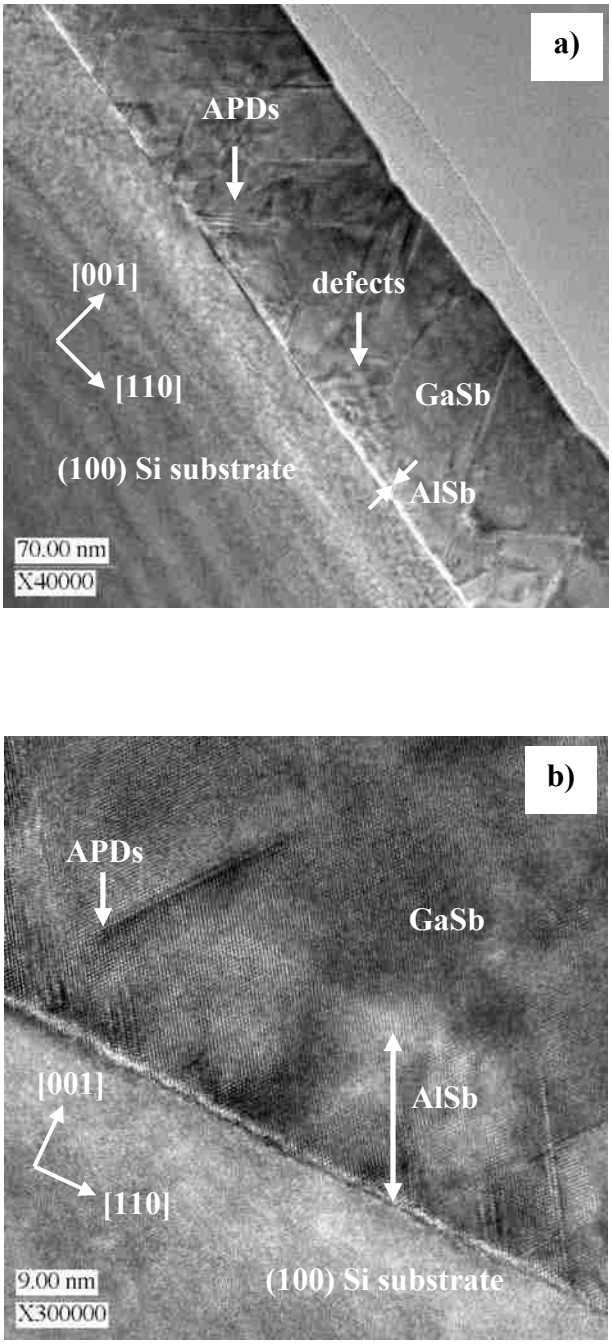

Figure 3.8: TEM images show the structure of 100 nm GaSb / 10 nm AlSb / Si surface (a) low-resolution, (b) high-resolution, indicating the formation of lots of APDs and defects after AlSb deposition on (100) Si substrate.

It is well known that Sb atoms can interdiffuse with Si atoms, especially at high temperature, through point defect diffusion mechanisms. To realize III-Sb growth on Si for the use of device integration, we should study whether Sb atoms diffuse into Si substrate.

We have carefully analyzed the atomic interdiffusion between the epilayers and Si substrate by Scanning Transmission Electron Microscope (STEM) images along the AlSb/Si interface. As we know, Z-contrast imaging is an atomic number sensitive technique with atomic resolution. These Z-contrast images were formed by the annular dark field (ADF) detector collecting low-angle elastically scattered electrons only.[21] Single atoms scatter incoherently and the image intensity is the total sum of the individual atomic scattering contributions. The local intensity of Z-contrast is normally proportional to the square of the average atomic number Z, i.e., which is related to chemical composition of samples.[22,23] Better image contrast can be obtained where a significant difference exits between the various epilayers. The average atomic number of Si, AlSb, and GaSb are 14, 32, and 41, respectively. Therefore, it is expected that GaSb have the highest Z-contrast intensity while Si has the lowest intensity for the same sample thickness.

Figure 3.9 shows the cross-sectional STEM image of the sample shown in Figure 3.8. Figure 3.9 (a) clearly indicates that the sample structure is 10 nm AlSb layer nucleated on Si surface, followed by the capped layer of GaSb. Meanwhile, the limited cross-sectional area sampled by high-resolution STEM image, shown in Figure 3.9 (b),

shows no indication of any strong bright spots in the Si substrate. Therefore, we conclude that no Sb diffuses into Si substrate.

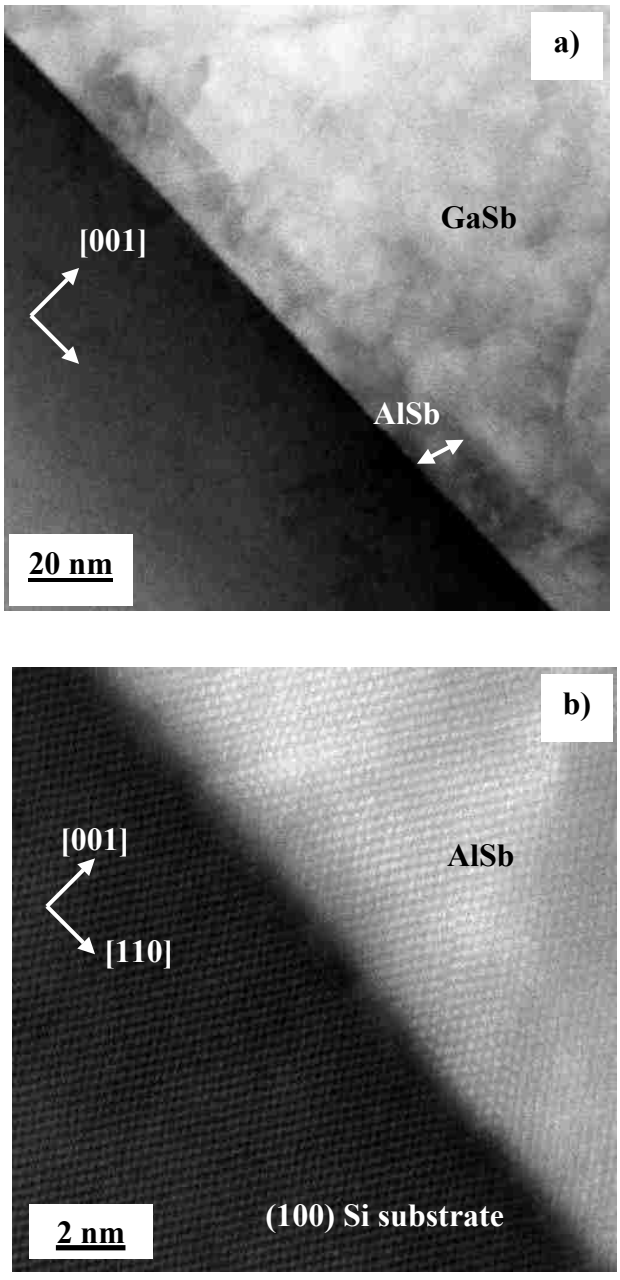

Figure 3.9: STEM images show the structure of 100 nm GaSb / 10 nm AlSb / Si surface (a) low-resolution, (b) high-resolution, indicating that there are no interdiffusion between the AlSb epilayer and (100) Si substrate.

3.3.3 AlSb on 5° miscut (100) Si

To improve the quality of the AlSb buffer on Si substrate, growth of III-V materials on miscut Si is a well-known solution for APD annhilation.[17,18] The use of misoriented substrates is essential for eliminating antiphase domains and stacking faults at the GaAs/Si interface.[8] The major reason of material improvement is due to the shortened (100) terraces formed by the miscut towards the (011). When the miscut angle is 2.5º to 5º towards the [110], the double atomic steps can present in miscut Si.[24] Therefore, the surface misorientation results in a high density of (100) terraces with double atomic steps, which shows that the surface layers on all terraces belong to the same Si sublattice, i.e., there are the same atomic arrangement at all terrace surface. Therefore, the two sublattices on the AlSb side are in registry again, then leading to the suppression of the APDs. The reduction of the APD density has been attributed to the formation of the double atomic steps in conjunction with an Al prelayer and strong Al-Sb strong bond prior to AlSb growth.

Under optimized growth conditions, we grow AlSb bulk layer on 5º miscut Si to simultaneously demonstrate low APD density and achieve a high quality IMF layer at the AlSb/Si interface. The growth is performed at a single temperature and has a very low defect density attributed to the IMF layer. The specific geometry of the 5˚ surface step seems to be well suited for IMF formation. In contrast, our previous attempts to form IMF on 3˚ miscut Si substrate did not produce a well-formed IMF, indicating sensitivity of the formation conditions.

The misfit array and resulting bulk materials have been analyzed carefully using low-resolution and high-resolution TEM images. Figures 3.10 (a) - (c), show high and low-resolution images of the AlSb/Si interface with the Si substrate having a 5º miscut towards the [110]. Figure 3.10(a) features a low-resolution image of bulk AlSb material, the Si substrate and the IMF. The bulk AlSb appears APD-free and defect-free. The IMF appears as periodic dark and light bands localized at the interface. The darker regions in this multi-beam image indicate a compressively strained atomic lattice relative to the surrounding material. The strained, dark areas appear elongated suggesting an asymmetric distribution of the strain-field amongst several atoms. This is different from our other studies involving AlSb on Si (001) and GaSb on GaAs, in which the dark strain-field images appear more circular and symmetric along the interface.[6] In the higher-resolution image of Figure 3.10(b), the periodic IMF and associated strain field appear as a wave-like distribution of contrasting dark and light regions. At even higher magnification, Figure 3.10(c), the atomic structure becomes clearer. Though the Si double steps are not discernable, the exact position of the misfit dislocations can be detected and marked with boxes. Two dislocations are specifically labeled by "1" and "2" for discussion. The Burger's circuit theory performed on this image shows that the Burger's vector, i.e., $\frac{a}{2}[110]$, lies along the interface and identifies these misfit as 90° pure edge type. The misfit separation, S, is measured to be ~ 3.46 nm and corresponds to exactly 8 AlSb lattice sites grown on 9 Si lattice sites.

This image provides details relating the IMF and step-edge to the resulting strain field. While misfit dislocation "1" is adjacent to a high strain region, misfit dislocation

"2" lies in a relatively low-strain region. We therefore surmise that the dark regions are perhaps associated with the step–edge and result from the strained Al-Al or Al-Si bonds along the [001] direction.

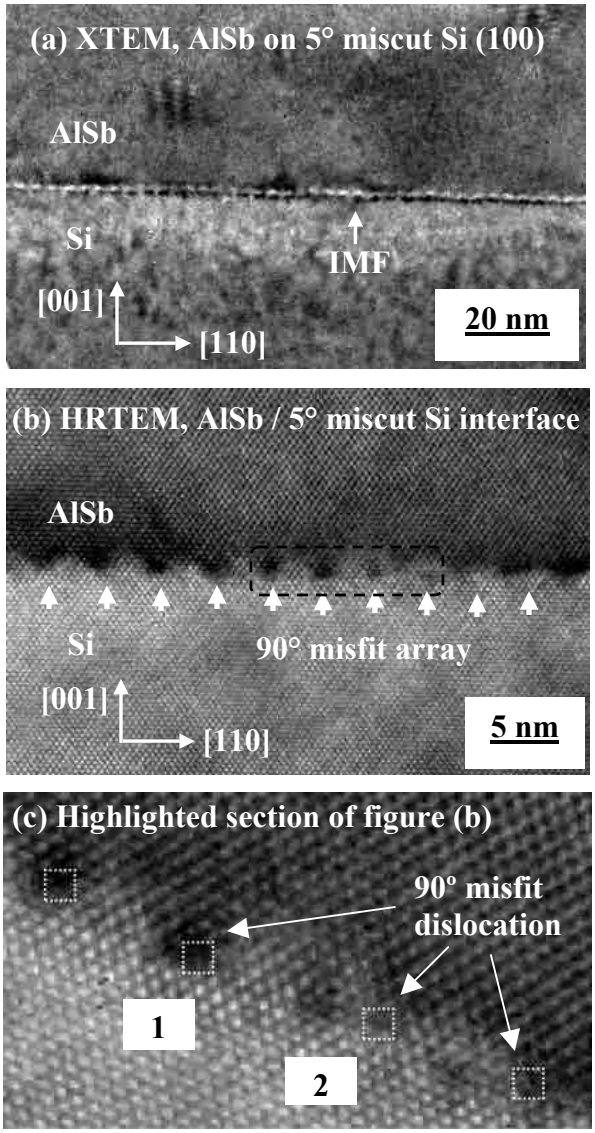

Figure 3.10: Cross-sectional TEM images of AlSb grown on 5° miscut Si (001) substrate under (a) low-resolution, (b) high-resolution conditions, and (c) highlighted section of figure (b), featuring the periodic IMF array. [25]

A schematic in Figure 3.11 illustrates a possible arrangement of step geometry and IMF location along with atomic alignment of the Al and Sb sublattices at the step edges forming the strain field.

(a) Step-geometry at 5° miscut AlSb/Si interface

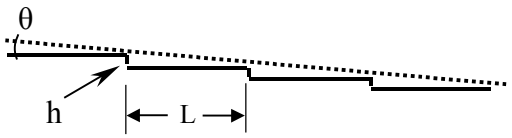

(b) Atomic alignment at 5° miscut AlSb/Si interface

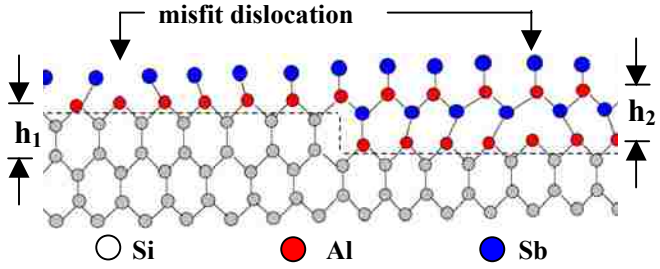

(c) Strain-fields at 5° miscut AlSb/Si interface

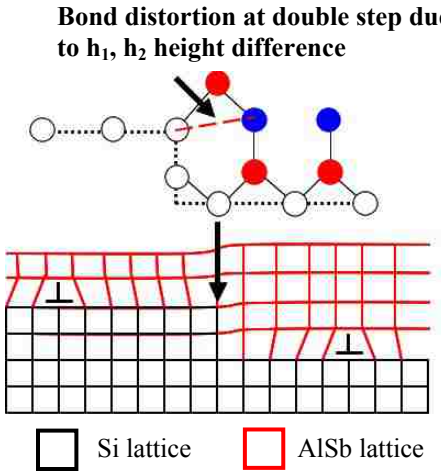

Figure 3.11: Series of schematics to eluciate atomic arrangement and resulting strain involved in AlSb on miscut Si. Part (a) shows the step geometry on a 5° miscut Si substrate. Part (b) shows a "ball and stick" schematic of Al, Sb and Si sublattices. Part (c) indicates sources of strain at the step edge due to the h_1, h_2 mismatch.

In Figure 3.11(a), the step length L is defined as $L = h \cdot cot\theta$ *where* h is the step height and θ is the miscut angle. The double atomic steps on 5 ˚ miscut Si (100) yields h = 2.72 Å, thus $L = h \cdot cot\theta = 2.72 \times cot5° = 31.09$ Å. This value is fairly well matched to IMF spacing, S and results in a single IMF per step. Figure 3.12(b) is a "ball and stick" schematic showing atomic arrangement of the AlSb and Si sublattices. Strain, indicated in the TEMs of Fig.3.10, is generated at the step edge due to the height differential between the Si double step, h_1 and the two-atom-layer height of AlSb, h_2, in the [100] direction. Using the following values of h_1=2.72 Å and h_2=3.06 Å, we calculate a height mismatch of 12.5% along the [100] direction. This causes the AlSb layer growing on the lower step to be compressed along the [100] direction to facilitate registration, resulting in a compressive strain along the [110] direction. The effect of this strain at the Si double-step is depicted in Fig 3.11(c). Since the miscut is 5º towards the [110] direction, we expect that this effect is only along [110] direction and is not repeated along the [1-10] direction.

The double step height, h, is obviously critical for achieving APD suppression on the miscut Si substrate. The importance of L relative to S, for high quality IMF formation, is suggested by a comparison of AlSb grown on 5˚ and 3˚ miscut substrates grown under similar conditions. Figure 3.12 (a) shows the AlSb bulk on 3° miscut Si (001) substrate along the [110] direction. The APDs and defects density are $>10^7$ /cm^2. Figure 3.12(b) shows the corresponding interfacial misfits using HRTEM image. For a 3˚ miscut, the step height may be a single or double step or a mixture. For a single step, h=1.35 Å, the step length, $L = h \cdot cot\theta = 1.35 \times cot3° = 25.72$ Å < S. For a double step,

h=2.72 Å, the step length, L = $h \cdot \cot\theta = 2.72 \times \cot 3° = 51.90$ Å $> S$. While we can not substantiate any required relations between L and S, a step length L that is significantly shorter or longer than the IMF spacing will increase the number of interaction points between the step edge and the 90˚ misfit which may initiate 60˚ misfit formation.

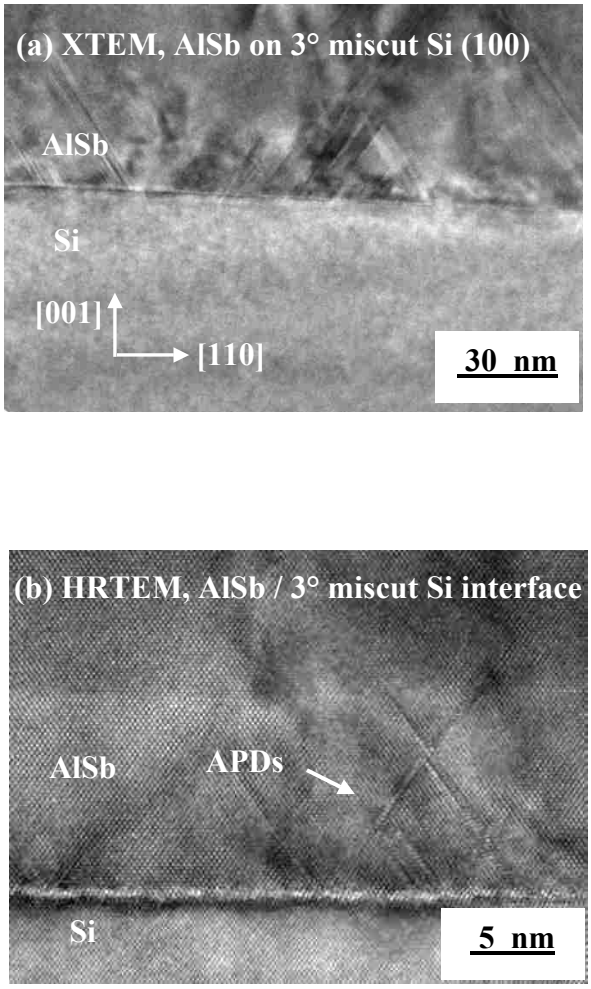

Figure 3.12: Cross-sectional TEM images of AlSb grown on 3° miscut Si (100) substrate under (a) low-resolution and (b) high-resolution conditions featuring defects and APDs. [25]

In order to understand the formation of IMF at the AlSb/Si interface, it is necessary to analyze the growth process. After the removal of the oxide remnants, the substrate temperature is reduced and stabilized at 510 °C followed by ~ 25 s Al soak and then 15 s soak in an Sb overpressure condition. As we know, compared to Si atom, Al atom has similar atomic size, which shows that it is possible for Al atom to replace the position of Si atom during the Al soak. It is worth mentioning that although Al-Si bond is larger (2.45 Å) than Si-Si (2.17 Å), but in $AlSi_2$ cluster the Al-Si bond shrinks significantly and it becomes almost equal to that of Si-Si bonds (2.36 for Al-Si and 2.38 for Si-Si).[26] The Al atom substitutes one of the Si atoms from the host Si cluster, only causing a small local distortion. The following Sb soak results in the antimony atoms forming a 2D reconstruction on the surface through an interfacial array of misfit dislocations.[12] This reconstruction involves the packing of the Sb atoms on the Si surface such that the Sb atoms skip every 9^{th} Si atom in the substrate. The subsequent growth of AlSb on Si results in interfacial misfit (IMF) array which is a completely relaxed growth mode with extremely low defect density. This effect occurs due to the fact that the Sb atom forms a good bond with the underlying Al atoms but does not react with the Si substrate to displace the Si atoms.

A schematic of the interfacial atoms at AlSb/Si interface in Figure 3.13 illustrates atomic arrangement and bonding in the (110) plane around the interfacial misfit. The characteristic and undistorted zinc-blende arrangement occurs exactly at 4^{th} atom from the misfit. These bonds appear undistorted between misfits, but begin bending and stretching until some physical limit surpassed to necessitate a skipped bond, i.e., misfit.

Therefore, the misfit is formed when the bond length becomes so large that the energetics of the system cannot accommodate that bond any more. Thus, the formation for the misfit array is a self-assembled process driven by energy minimization.

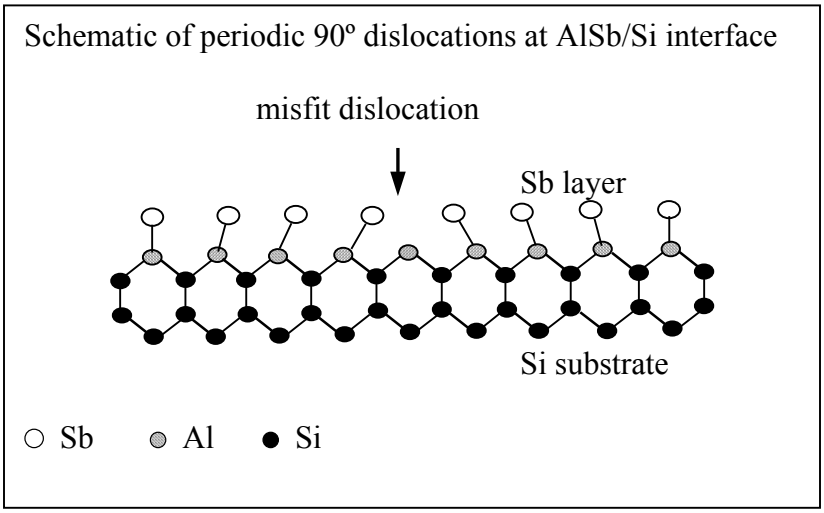

Figure 3.13: Schematic of a 90° misfit array array at AlSb/Si interface.

In conclusion, we have identified the growth mechanisms of highly mismatched AlSb on 5° miscut Si substrate. Our analysis indicates that the 5º miscut allows the formation of a single 90º misfit dislocation per step thus resulting in the isolation of the misfit dislocations from each other, then the strain does not build up and the high strain energy due to large mismatch is relieved.

3.4 Defect analysis and density measurement by TEM

To verify the quality of the AlSb epilayer on 5° miscut Si substrate, we use TEM plan-view images to measure the dislocation density. The experimental results, shown in Figure 3.14 (a) and (b), indicate that the AlSb bulk layer grown on 5° miscut Si (100) substrate has very low density of APDs, compared to that grown on Si (100) substrate. The average surface roughness of AlSb bulk layer grown on 5° miscut Si (100) substrate is only ~0.6 nm, indicating a good surface quality. Similarly, plan-view TEM image, shown in Figure 3.15, displays also very low density of anti-phase boundaries (APBs) on the surface. This is attributed to the formation of double-atomic steps during the in-situ cleaning of the Si wafer in the case of 5° misorientations in the [110] direction, thus leading to suppress the APDs.

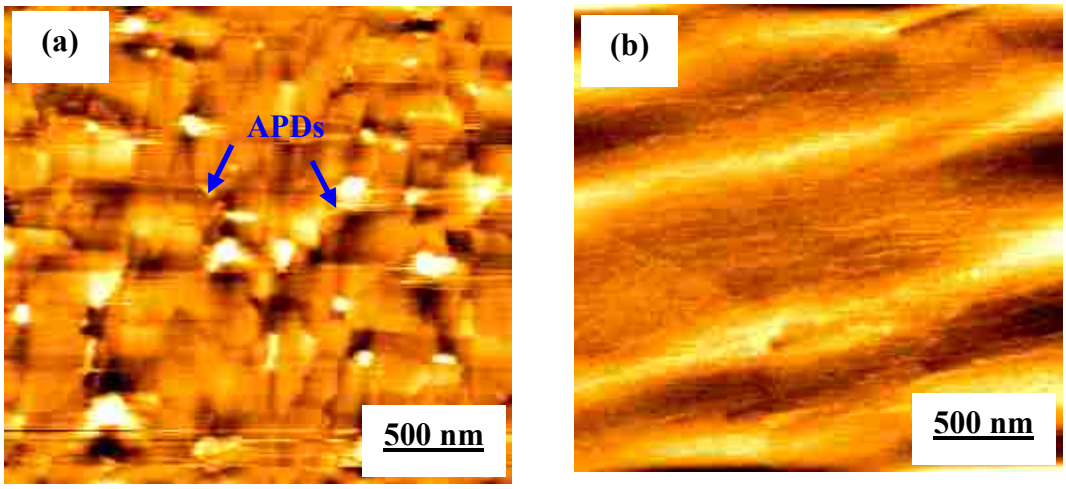

Figure 3.14: AFM images of the 1 µm GaSb grown on AlSb on (a) Si (001) surface, (b) 5° miscut Si surface, indicating the use of misoriented substrates is essential for the suppression of antiphase domains.

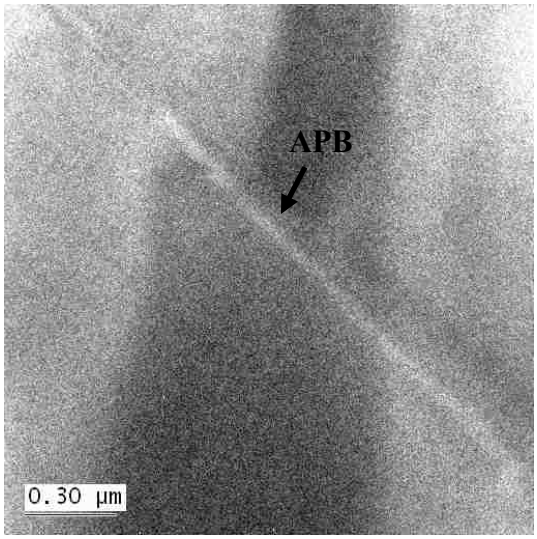

Figure 3.15: Plan-view TEM image of the GaSb surface grown on AlSb on 5° miscut Si surface, indicating one of APBs on the surface, with very low APD density.

Surface analysis enables the calculation of dislocation and APD density in bulk GaSb grown on the AlSb/Si IMF under optimized growth conditions. The dislocation density is best verified by plan-view TEM images. Figure 3.16 (a) and (b) show plan-view TEM images of GaSb bulk material (1 µm) on AlSb (50 nm)/ 5° miscut Si. Figure 3.16 (a) features visible defects at the surface. This image, captured from an edge region where growth conditions are perhaps not optimum, indicate our characterization capability to capture defects if they exist. Figure 3.16 (b) shows the center surface area with no defects. Based on scanning different areas of the center of the wafer we estimate our defect density to be ~ 7×10^5 defects/cm^2. The images further show that the AlSb bulk layer grown on 5° miscut Si planes is APD free. This is also verified in Figure 3.17

which shows a 4 μm x 4 μm AFM image of the same sample, indicating no APDs visible in the scan.

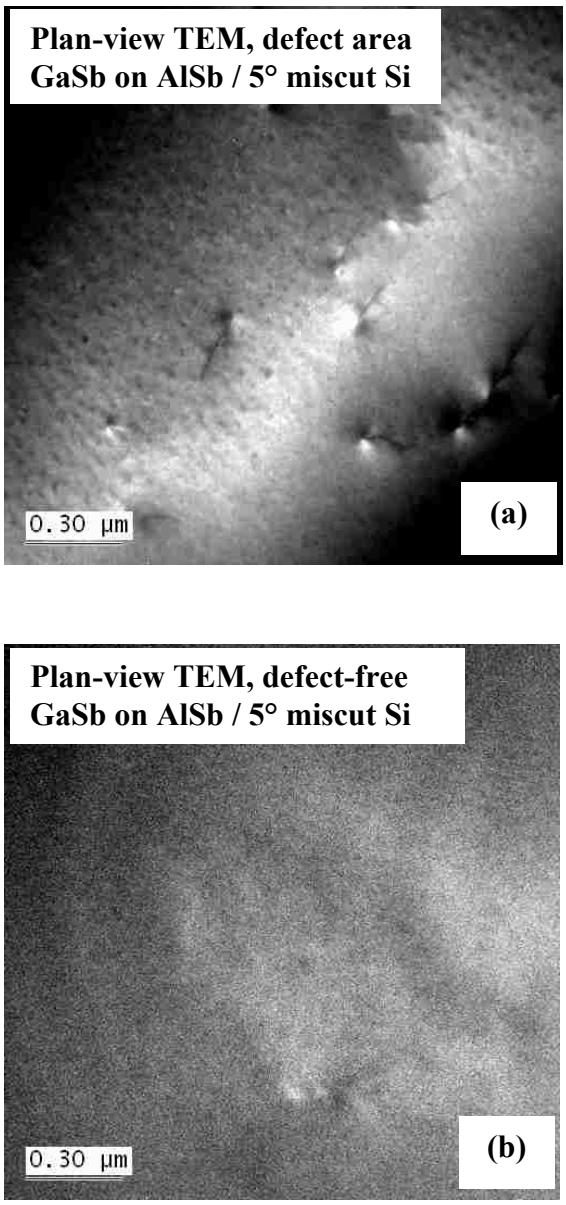

Figure 3.16: Plan-view TEM image of the GaSb surface grown on AlSb on 5° miscut Si surface, a) defect surface area, b) perfect surface area, indicating very low defect density.

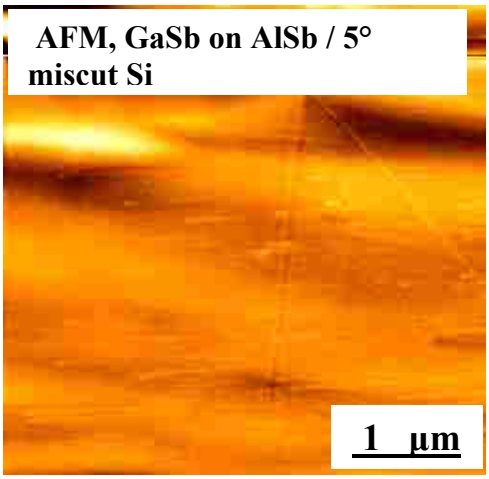

Figure 3.17: AFM image of 1µm GaSb grown on AlSb on 5° miscut Si surface

3.5 Applications of AlSb/Si IMF

Using IMF growth techniques, we demonstrated room temperature photopumped (PP) operation lasing of a GaSb quantum well (QW) based VCSEL monolithically grown on Si (100) substrate. The VCSEL epitaxial structure is shown in Figure 3.18.

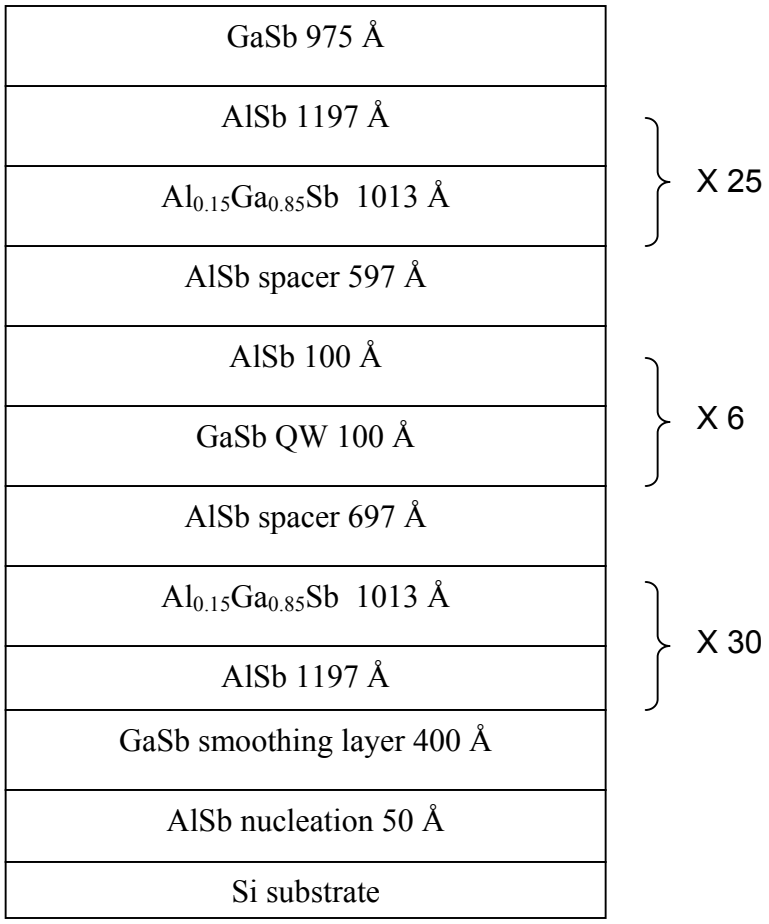

Figure 3.18: Schematic of monolithic VCSEL structure shows GaSb/AlSb QWs in half-wave cavity surrounded by AlGaSb/AlSb DBRs. [27]

Figure 3.19 shows room-temperature photo-pumped lasing results at 1.65 μm from VCSEL grown on Si substrate. Figure 3.19 (a) is the light-in against light-out (L-L)

curve with peak threshold intensity, I_{th} = 0.1 mJ/cm^2, and Figure 3.19 (b) shows spectra for different pump intensities from subthreshold to lasing at 0.4 × I_{th} , 1.0 × I_{th} and 1.1 × I_{th}.

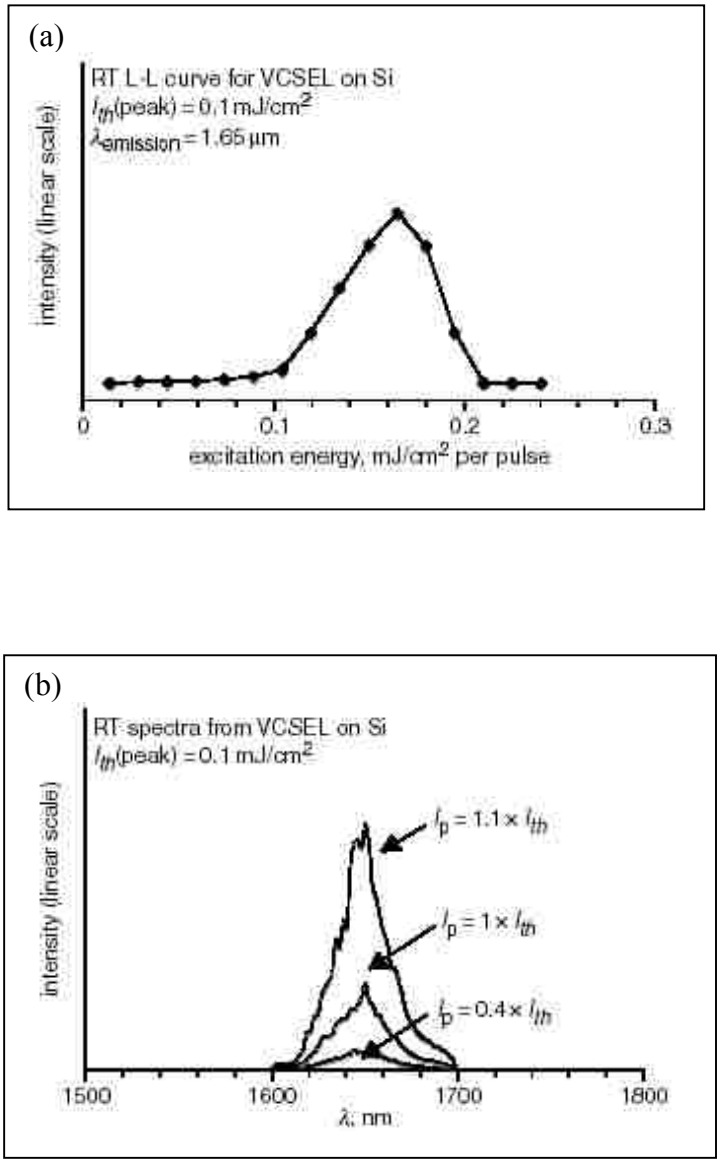

Figure 3.19: RT-PP VCSEL lasing at 1.65 µm, (a) L-L curve indicating threshold intensity at pump power of 0.1 mJ/cm^2 per pulse, (b) Spectra at pump intensities – 0.4 × I_{th} , 1.0 × I_{th} and 1.1 × I_{th}. [27]

3.6 Summary

We analyzed the growth processes of AlSb grown on Si (100) and 5° miscut Si (100) substrates. We demonstrated that the interfacial misfit (IMF) array in the growth of highly mismatched ($\Delta a_0/a_0$=13%) AlSb bulk layers can be formed on both of Si (100) and 5° miscut Si (100) substrates. However, a 5° miscut Si (001) substrate can provide the effect of suppress of APDs. Under optimized growth conditions, strain energy from the AlSb/Si interface is accommodated by a 90° interfacial misfit dislocations resulting in very low defect density and the suppression of APDs, confirmed by plan-view TEM images. High-resolution TEM image indicates that the misfit array at the AlSb/Si interface has a period of ~ 3.46 nm, according to 8 AlSb atoms grown on 9 Si atoms. We attribute the success of AlSb growth on Si surface to both the step doubling-atom mechanism in combination with the strong Al-Sb atomic bond. The AlSb bulk materials with low dislocation density and strain-relieved properties generated by the growth conditions can provide a promising technology for the monolithic integration of III-V devices on Si substrate.

References for chapter three:

[1] K.K. Linder, J. Phillips, O. Qasaimeh, X.F. Liu, S. Krishna, P. Bhattacharya, and J.C. Jiang, Appl. Phys. Lett. **74**, 1355 (1999).

[2] D.G. Deppe, N. Jr. Holonyak, D. W. Nam, K. C. Hsieh, G. S. Jackson, R. J. Matyi, H. Shichiujo, J. E. Epler, and H. F. Chung, Appl. Phys. Lett. **51**, 637 (1987).

[3] D. G. Deppe, N. Chand, J. P. van der Ziel, and G. J. Zydzik, Appl. Phys. Lett. **56**, 740 (1990).

[4] D. G. Deppe, N. Jr. Holonyak, K. C. Hsieh, D. W. Nam, and W. E. Plano, Appl. Phys. Lett. **52**, 1812 (1988).

[5] O. Kwon, J. J. Boeckl, M. L. Lee, A. J. Pitera, E. A. Fitzgerald, and S. A. Ringel, J. Appl. Phys. **100**, 013103 (2006).

[6] M. E. Groenert, C. W. Leitz, A. J. Pitera, V. Yang, H. Lee, R. J. Ram, and E. A. Fitzgerald, J. Appl. Phys. **93**, 362 (2003).

[7] Z. Mi, P. Bhattacharya, J. Yang, and K. P. Pipe, Electron. Lett. **41**, 742 (2005).

[8] Z. Mi, J. Yang, P. Bhattacharya, and D. L. Huffaker, Electron. Lett. **42**, 121, (2006).

[9] A. Georgakilas, P. Panayotatos, J. Stoemenos, J.-L. Mourrain, and A. Christou, J. Appl. Phys. **71**, 2679 (1992).

[10] J. C. C. Fan and J. M. Poate, Eds., Heteroepitaxy on Silicon. vol. **67**, Pittsburgh, PA: Materials Research Society, (1986).

[11] H. K. Choi, R. Hull, H. Ishiwara, and R. J. Nemanich, Eds., Heteroepitaxy on Silicon: Fundamentals, Structure and Devices, vol. **116**, Pittsburgh, PA: Materials Research Society, (1988).

[12] S. H. Huang, G. Balakrishnan, A. Khoshakhlagh, A. Jallipalli, L.R. Dawson, and D.L. Huffaker, Appl. Phys. Lett. **88**, 131911 (2006).

[13] M. Mehta, G. Balakrishnan, S. H. Huang, L.R. Dawson, and D.L. Huffaker, Appl. Phys. Lett. **89**, 211110 (2006).

[14] V. Kumar and B. S. R. Sastry, Cryst. Res. Technol. **36,** 565**,** (2001).

[15] J. P. van der Ziel, R. J. Malik, J. F Walker, and R. M. Mikulyak, Appl. Phys.Lett. **48**, 454 (1986).

[16] K. Akahane, N. Yamamoto, S. Gozu, and N. Ohtani, J. Cryst. Growth. **264**, 21 (2004).

[17] H. Kroemer, *Mat. Res. Soc. Proc.* Vol. **67**, 3 (1986).

[18] J. S. Harris, Jr. S. M. Koch and S. J. Rosner, *Mat. Res. Soc. Proc.* Vol. **91**, 3 (1987).

[19] T. Sakamoto and G. Hashiguchi, Japan, J. Appl. Phys. **25**, L57 (1986).

[20] P. N. Uppal and H. Kroemer, J. Appl. Phys. **58**, 2195 (1985).

[21] D. B. Williams and C. Barry Carter, Transmission Electron Microscopy, Kluwer Academic/Plenum, New York, 1996.

[22] P. D. Nellist and S. J. Pennycook, J. Microsc. **190,** 159 (1998).

[23] H. Lakner, B. Bollig, S. Ungerechts, and E. Kubalek, J. Phys. D **29**, 1767 (1996).

[24] L. Barbier, A. Khater, B. Salanon, and J. Lapujoulade, Phys. Rev. B **43**, 14730 (1991).

[25] S. H. Huang, G. Balakrishnan, A. Khoshakhlagh, P. Li, L.R. Dawson, and D.L. Huffaker, submitted to Appl. Phys. Lett., Apr. 2007.

[26] S. Nigam, C. Majumder, and S. K. Skulshreshtha, J. Chemical Physics **121**, 7754 (2004).

[27] G. Balakrishnan, S. H. Huang, A. Khoshakhlagh, A. Jallipalli, P. Rotella, A. Amtout, S. Krishna, C. P. Haines, L.R. Dawson, and D.L. Huffaker, IEE Electron. Lett. **42**, 6 (2006).

Chapter 4

Interfacial misfit based GaSb QDs on GaAs substrate

4.1 Introduction

Lattice-mismatched epitaxy of Sb-based materials on GaAs substrate has attracted considerable attention because of the lots of advances in optoelectronic devices, including detectors, integrated laser, solar cells, and transistors.[1,2] Especially, GaSb quantum dots (QDs) in a GaAs matrix have drawn recent attention for their potential ability to demonstrate QD-based emitters at the technologically important wavelength of 1.55 μm along with their unique electronic and optical properties caused by their staggered (type-II) band alignment and large valence band offset.[3] The type-II staggered active region can be designed to work at different wavelengths by varying the matrix composition surrounding GaSb QDs. These types of active regions have been shown to work very effectively in the mid-IR (MWIR).[4] GaSb/GaAs QDs can also be used for demonstrating similar results in the near-IR, where no type-II devices have yet been demonstrated. In these type-II QDs, holes can be confined within QDs, while electrons produce quantum shell around QDs by the Coulomb interaction. Thus, they could be also useful for single carrier, even unipolar storage devices such as optical memory due to their longer radiative recombination lifetime.

To date, several groups have reported formation and optical properties of type-II GaSb/GaAs QDs using the Stranski-Krastanov (SK) growth mode with demonstrations of light emission from QDs and their wetting layers.[5,6,7,8] According to its definition, the SK growth mode of GaSb/GaAs leads to highly strained QDs, which is somewhat of a hindrance in device realization since it limits both peak wavelength (up to ~1.2 μm) and dense stacking.

The two-dimensional IMF, formed at the heterointerface between the epilayer and substrate, relieves strain energy due to high lattice mismatch and has been noted to form a wide range of surface phenomena from strain-free islands to highly planar strain-free, defect free bulk material.[9,10] However, the strain-free properties of the IMF growth mode are extremely attractive for QD growth process since it becomes possible for dense QD stacking with a thinner spacer, compared to SK QDs. The growth of IMF GaSb QDs has not been as straightforward as that of conventional InAs/GaAs QDs due to the rather narrow V/III ratio window and therefore not as well studied.[11] The possibility for dense stacking of IMF GaSb QDs can prove beneficial for QD sensors, emitters and solar cells.

In this chapter, we demonstrate the ability to grow GaSb QDs in IMF growth mode as well as the SK growth mode by varying V/III ratio, and study further the formation of IMF QDs within a narrow V/III ratio, along with electronic and optical properties of strain-relieved densely stacked IMF GaSb QDs.

4.2 Formation of interfacial misfit array based GaSb QDs

In the GaSb/GaAs IMF QD formation, the samples are grown on semi-insulating GaAs (001) substrates by MBE VG80 reactor with a 100 nm GaAs buffer. The GaSb QDs are formed at 510 °C on the As-rich GaAs surface with a growth rate of 0.32 monolayers (MLs)/s with V/III ratio = 10 for IMF mode. The samples for microscopic characterization are immediately cooled to room temperature. As for the PL characterization, the sample includes an $Al_{0.9}Ga_{0.1}As$/GaAs barrier surrounding the single GaSb QD layer active region and a GaAs capped layer without growth interruption.

Figure 4.1 shows an AFM image of GaSb IMF QD ensembles on GaAs substrate. The IMF QDs are elongated slightly along the [1-10] direction in comparison with the [110] direction. The QD dimensions are widely varied with an average length, width, and height of 50 nm, 30 nm, and 6 nm, respectively. The QD density is about 6×10^{10} QDs/cm^2.

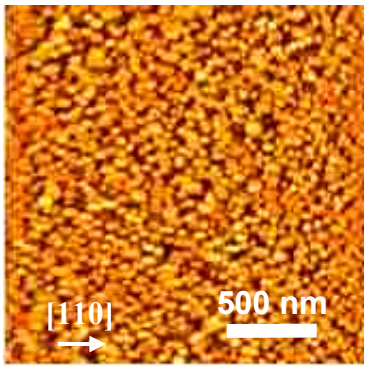

Figure 4.1: AFM image of GaSb IMF QDs on GaAs substrate after 3 ML deposition.

Figure 4.2 shows a cross sectional TEM image of single IMF GaSb QD and the characteristic array of misfits at the GaSb/GaAs interface. The shape of IMF QD is very flat and broad. The QD height and width are 5 nm and 30 nm, respectively, in agreement with the results of AFM image shown in Figure 4.1. The dark line in Figure 4.2 shows the native oxide formed on the sample between growth and analysis. The characteristic array of misfits can be observed at the GaSb/GaAs interface, where the spacing between the misfit dislocations is ~ 5.6 nm, corresponding to 13 GaSb lattice sites or 14 GaAs lattice sites.

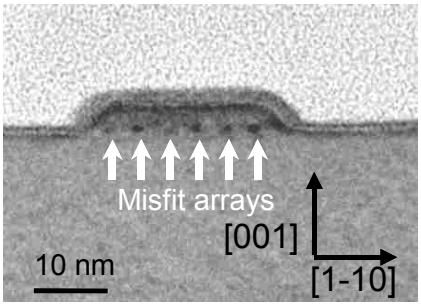

Figure 4.2: XTEM image of 3 ML GaSb IMF QDs on GaAs substrate.

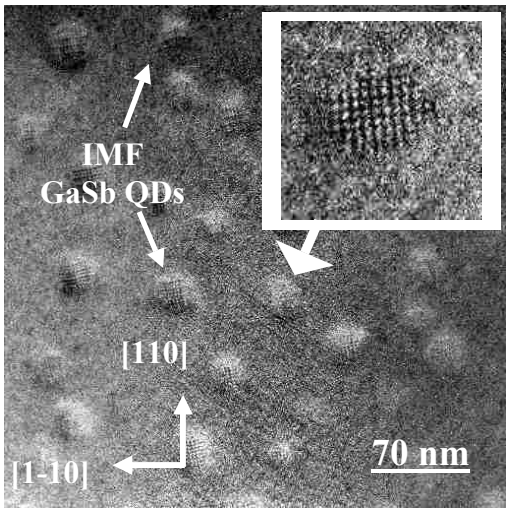

Figure 4.3: Plan-view TEM image of 3 ML GaSb IMF QDs on GaAs substrate.

Figure 4.3 displays the [001] bright field plan-view TEM image of GaSb IMF QDs on GaAs after 3 ML deposition. The misfit dislocations form at both [110] and [1-10] directions simultaneously, which indicates the presence of IMF array at the GaSb/GaAs interface.

4.3 Formation of Stranski-Krastanov GaSb QDs

In the GaSb/GaAs SK QD formation, the growth conditions are the same as that of IMF growth mode, with exception of the V/III ratios during the QD formation. The samples are grown on semi-insulating GaAs (001) substrates by MBE VG80 reactor with a 100 nm GaAs buffer followed by the QD ensemble. The GaSb QDs are formed at 510°C with a total coverage of 3 ML, a growth rate of 0.3 MLs/s with V/III ratio = 1 for SK growth mode. Figure 4.4 shows an AFM image of GaSb SK QD ensemble on GaAs substrate. The SK QD ensemble shows typical characteristics for SK QDs with an average width and height of 10 and 5 nm, respectively. The QD density is about 3×10^{10} QDs/cm^2.

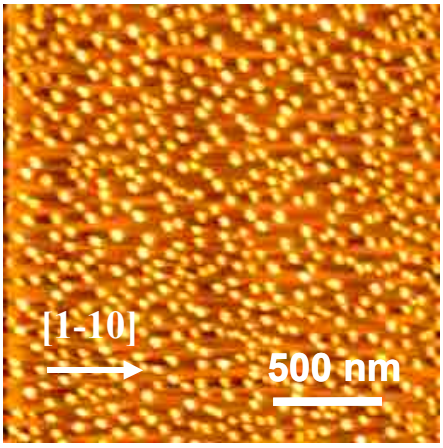

Figure 4.4: AFM image of GaSb SK QDs on GaAs substrate after 3 ML deposition.

Figure 4.5 shows a high-resolution cross sectional TEM image of SK GaSb QD on GaAs substrate, indicating a highly crystalline SK QD with height and width of 7 nm and 10 nm, respectively, and a domelike shape typical of SK-formed QDs. This images also clearly shows that the GaSb/GaAs interface is abrupt and no indication of misfit dislocations exist at the heteointerface.

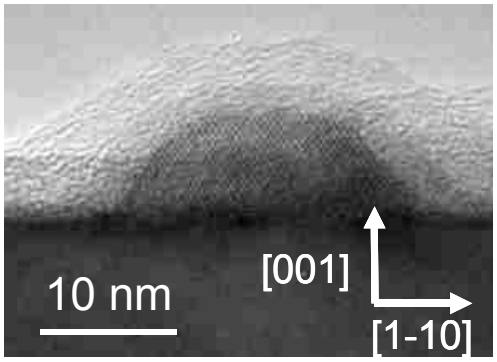

Figure 4.5: XTEM image of GaSb SK QDs on GaAs substrate after 3 ML deposition.

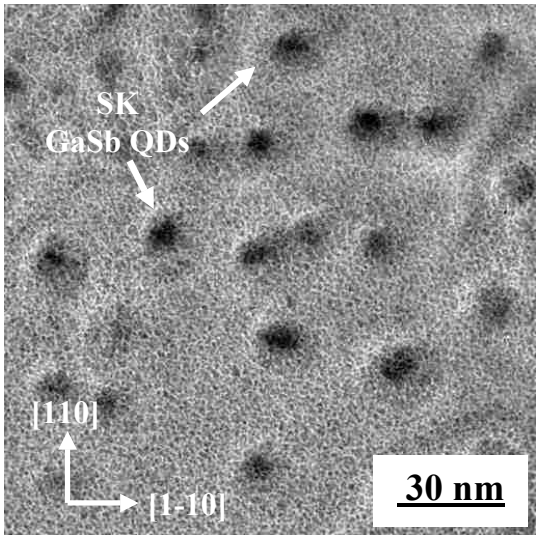

Figure 4.6: [001] bright field plan-view TEM image of 3 ML GaSb SK QDs on GaAs substrate.

Figure 4.6 indicates the [001] bright field plan-view TEM image of 3ML GaSb SK QD on GaAs substrate. This plan-view image shows the absence of misfit dislocations at the GaSb/GaAs interface, indicating that these SK QDs are highly strained. The QDs base is roughly circular, and the QD size is ~10 nm.

4.4 Optical properties of IMF QDs and SK QDs

Firstly, we study the effect of V/III ratio on the optical properties of GaSb QDs. The RT PL spectra for both IMF and SK ensembles with a total coverage of 4 ML are collected using a conventional PL setup with an excitation by either a He-Ne or Ar+ laser with a 2 mm spot size. Figure 4.7 shows the RT PL spectra of GaSb QDs with an excitation by a He-Ne laser at V/III ratios of ranging from 1 to 6.5. When the V/III ratio of GaSb growth is ~1, PL spectra show weak light emission near 1.14 μm with a FWHM of 64 meV from highly-strained SK QDs. Emission from large bulk-like GaSb islands at 1.66 μm is also measured due to the coalescence of neighboring dots by an excess of GaSb materials. When the V/III ratio is more than 2, the PL peak of GaSb QDs shifts abruptly towards 1.3 μm (FWHM of ~ 53 meV) due to the transition from strained SK to unstrained IMF growth mode. Moreover, by further increasing the V/III ratio from 2 to 6.5, the PL peak shifts towards longer wavelength from 1.34 μm to 1.39 μm, and the PL intensity decreases dramatically. The reason is that an excess of Sb atoms during the formation of GaSb QDs increases Sb intermixing from GaSb QD layers into GaAs matrices, resulting in the extended wavelength, increased lattice mismatch and strain in

the barriers. Therefore, the Sb-rich growth condition leads to strain related defects and reduces PL intensity.

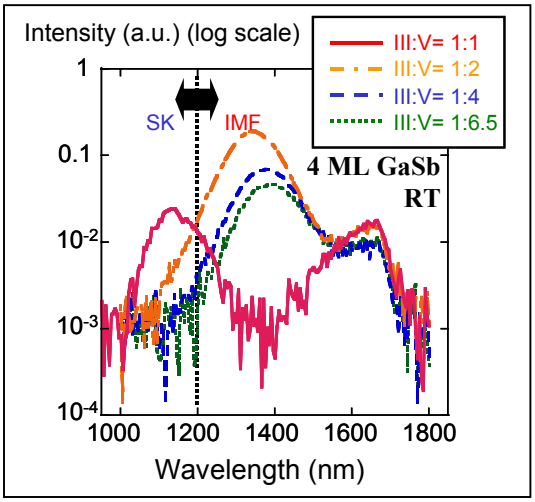

Figure 4.7: RT PL spectra of single layer of GaSb QDs at different V/III ratios ranging from 1 to 6.5. The PL peak and FWHM of GaSb QDs at V/III ratios of 1, 2, 4, or 6.5 are 1.14 µm and 64 meV; 1.34 µm and 53 meV; 1.38 µm and 56 meV; and 1.39 µm and 53 meV, respectively. [12]

Secondly, we analyze the effect of GaSb coverage on the optical properties of GaSb QDs. Figure 4.8 shows the PL spectra of GaSb QDs with a V/III ratio of 2 with an excitation by Ar+ lasers (0.58 W) at total GaSb coverage ranging from 2 to 6 ML at RT. When the GaSb coverage is 2 ML, very weak PL can be observed at 1.12 µm. By increasing the GaSb coverage, the PL peak shifts towards longer wavelength over 1.3 µm, and the peak intensity increases dramatically. In addition, we observed the excited state of GaSb QDs at 1.13 µm which grows with higher pump powers as the lower states fill.[13] Meanwhile, light emission from large bulk-like GaSb islands at 1.66 µm is also observed here. We also note a second order GaAs peak that is visible at 1.75 µm at higher

excitation by Ar+-lasers. However, increased GaSb coverage results in planar growth and semi-two-dimensional GaSb layers using the IMF.

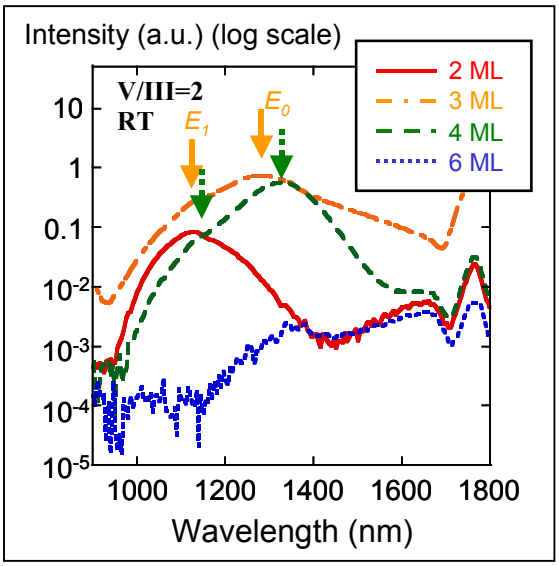

Figure 4.8: RT PL spectra of single layer of GaSb QDs with V/III ratio of 2 at a total coverage ranging from 2 to 6. The PL peak of GaSb QDs at a total coverage of 2, 3, 4, and 6 ML are 1.12 µm, 1.28 µm, 1.33 µm, and 1.35 µm, respectively. [12]

In order to grow dense QDs and increase the density of QDs in the active region of devices, the formation of multistacked GaSb QDs is a good choice. We grew ten stacked GaSb QD layers separated by 15 nm GaAs spacer layers with V/III ratio of 2 and 6.5. Figures 4.9 (a) and (b) show the cross sectional TEM images of the stacked structure with V/III ratio of 2 and 6.5, respectively. Figure 4.9 (a) indicate that low V/III ratio has the effect of suppressing Sb segregation, and produces smooth morphology and low defect density. The inset of Figure 4.9 (a) shows the high resolution TEM image of the first stacked QD layer, indicating a good quality of GaSb QD on GaAs. On the other

hand, high V/III ratio results in high Sb segregation, rough morphology at the interface, and threading dislocations, as shown in Figure 4.9 (b).

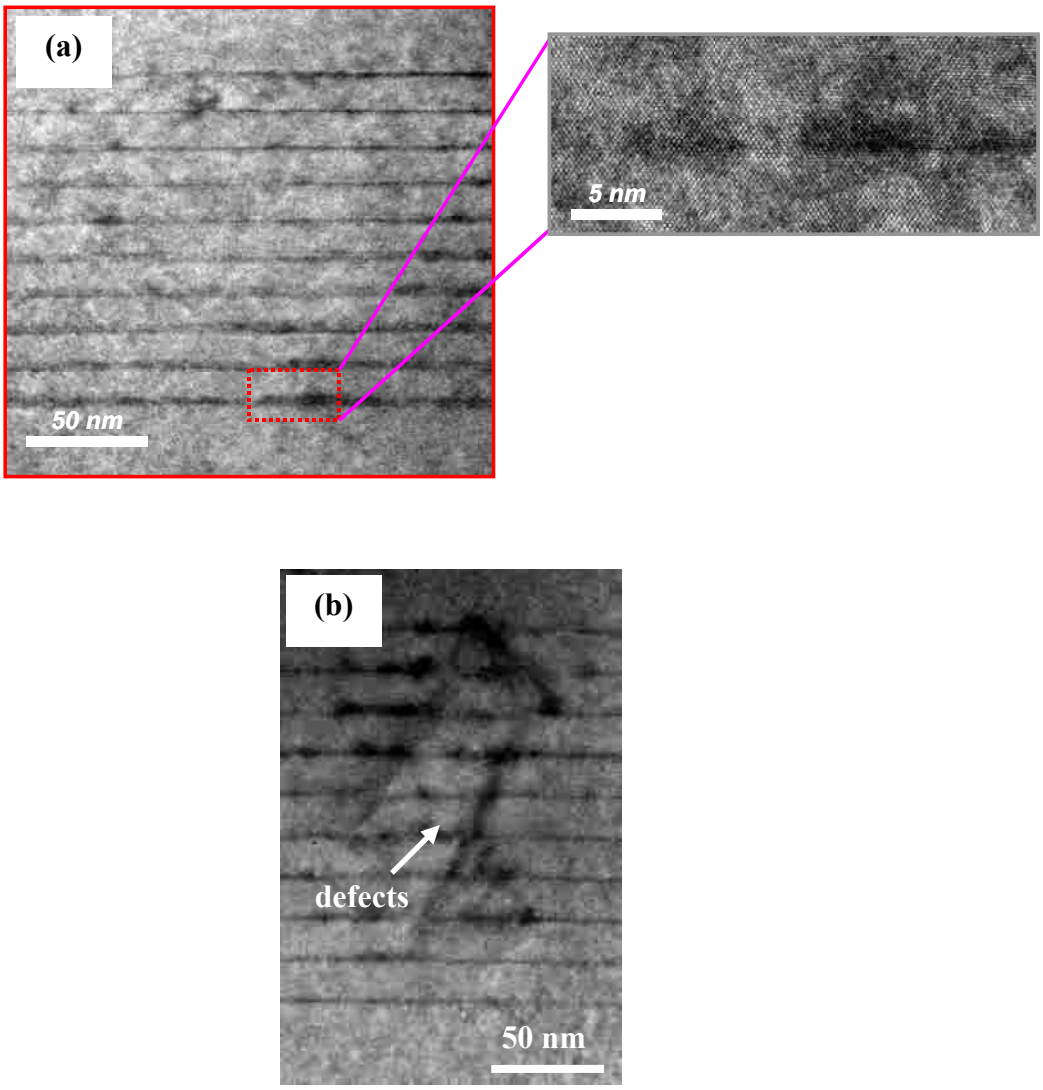

Figure 4.9: Cross sectional TEM images of 10 stacked GaSb QDs with V/III ratio of (a) 2, and (b) 6.5 at a total coverage 4 ML.

Optical characteristics and XRD analyses of ten stacked GaSb QDs separated by 15 nm GaAs spacer layers are also studied at RT with an excitation by Ar+ laser. Figure

4.10 shows the PL spectra of ten stacked GaSb QDs with V/III ratios of (i) 2 and (ii) 6.5. The PL spectrum with a higher V/III ratio shows very low PL intensity because an excess of Sb adatom within stacked ensembles causes the formation of large defects, resulting in surface undulations after stacking QDs or the formation of threading dislocations. On the other hand, the PL spectrum with a low V/III ratio displays improved PL intensity due to the improved crystalline quality of stacked QD ensembles by the suppression of Sb segregation, reduced defect formation and threading dislocations. Strong PL at 1.34 μm from ten stacked GaSb QDs is obtained at RT with a FWHM of 104 meV.

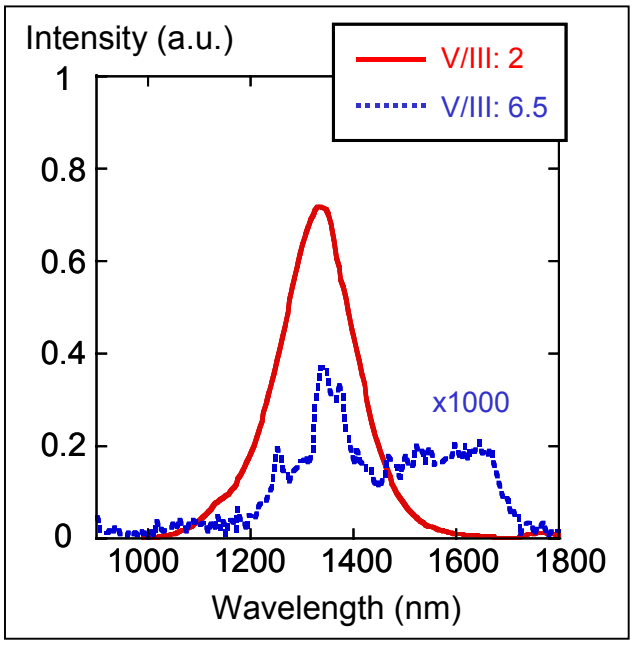

Figure 4.10: RT PL spectra of 10 stacked GaSb QDs at different V/III ratios (2 and 6.5). The spacer thickness between each QD layer is 15 nm. [12]

Figure 4.11 shows XRD spectra from ten stacked GaSb QDs with V/III ratios of (i) 2 and (ii) 6.5 using symmetric scans around (004) reflection in ω/2θ geometry. Improved crystalline quality is evident in the narrowing FWHM of the zero-order peak from (i) 330 arcsec to (ii) 103 arcsec by decreasing the V/III ratio during the growth of GaSb QDs, which elucidates the reduction of the formation of threading dislocations or defects.

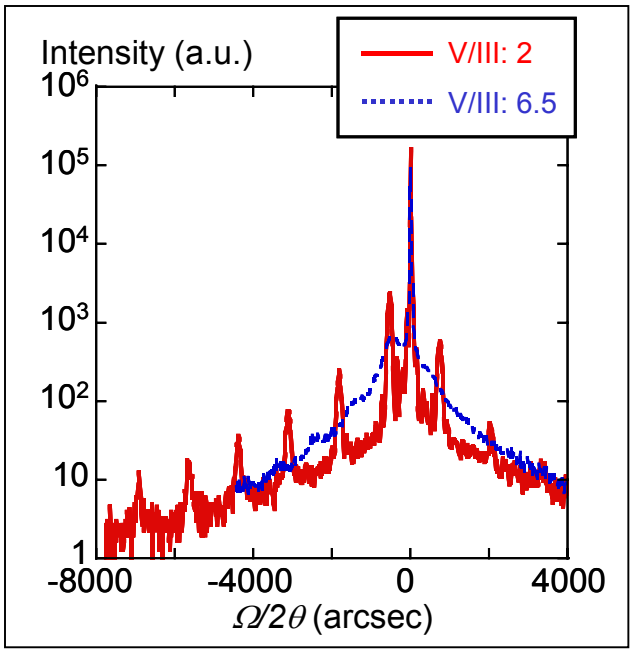

Figure 4.11: Symmetric 004 x-ray diffraction pattern for ten stacked GaSb QDs at different V/III ratios (2 and 6.5). [12]

4.5 Summary

We have demonstrated the ability to select either an IMF or a SK growth mode to grow GaSb QDs on GaAs substrates by varying the V/III ratio. A high V/III ratio such as

10:1 leads to IMF growth mode, while a low V/III ratio of 1:1 favors the SK growth mode. Both AFM and TEM images have verified the structural contrast in the two growth modes.

In the growth of GaSb/GaAs QDs, a moderate V/III ratio ($2 \leq V/III < 6.5$) produces strained-relieved QDs by IMF emitting at over 1.3 μm. Further increases in the V/III ratio lead to Sb segregation with the associated defects and threading dislocations.

We have formed high crystalline quality of 10 stacked, strain-relieved, and densely packed GaSb QDs by optimizing the V/III ratio of GaSb QD growth.

References for chapter four:

[1] S. M. Sze, Semiconductor Devices, Wiley, New York, (2002).

[2] R.J. Malik, J.P. van der Ziel, B.F. Levine, C.G. Bethea, J. Walker, J. Appl. Phys. **59**, 3909 (1986).

[3] G. A. Sai-Halasz, L. L. Chang, J. M. Welter, C. A. Chang, and L. Esaki, Solid State Commun. **27**, 935 (1978).

[4] J. R. Meyer, C. A. Hoffman, F. J. Bartoli, and L. R. Ram-Mohan, Appl. Phys. Lett. **67**, 757 (1995).

[5] E. R. Glaser, B. R. Bennett, B. V. Shanabrook, and R. Magno, Appl. Phys. Lett. **68**, 3614 (1996).

[6] B. R. Bennett, B. V. Shanabrook, and R. Magno, Appl. Phys. Lett. **68**, 958 (1996).

[7] L. Müller-Kirsch, R. Heitz, A. Schliwa, O. Stier, D. Bimberg, H. Kirmse and W. Neumann, Appl. Phys. Lett. **78**, 1418 (2001).

[8] M. Geller, C. Kapteyn, L. Müller-Kirsch, R. Heitz, and D. Bimberg, Appl. Phys. Lett. **82**, 2706 (2003).

[9] A. Yu Babkevich, R. A. Cowley, N. J. Mason and A. Stunault, J. Phys. Condens. Matter **12**, 4747 (2000).

[10] S. H. Huang, G. Balakrishnan, A. Khoshakhlagh, A. Jallipalli, L. R. Dawson, and D. L. Huffaker, Appl. Phys. Lett. **88**, 131911 (2006).

[11] A. Trampert, K. H. Ploog, and E. Tournie, Appl. Phys. Lett. **73**, 1074 (1998).

[12] J. Tatebayashi, A. Khoshakhlagh, S. H. Huang, L. R. Dawson, G. Balakrishnan, and D. L. Huffaker, Appl. Phys. Lett. **89**, 203116 (2006).

[13] G. Balakrishnan, J. Tatebayashi, A. Khoshakhlagh, S. H. Huang, A. Jallipalli, L. R. Dawson, and D. L. Huffaker, Appl. Phys. Lett. **89**, 161104 (2006).

Chapter 5

Conclusions

An interfacial misfit (IMF) array based growth mode has been demonstrated between GaSb and GaAs, and AlSb on Si substrate. This growth mode has resulted in epilayer materials with extremely low defect density grown on GaAs, GaSb and Si substrates.

Not only have we demonstrated that a periodic array of 90° misfit array can be formed under optimized growth parameters to fully relieve strain energy for compressive GaSb epilayer on GaAs, but also verified that a period 90° misfit dislocation array can be formed in the tensile GaAs epilayer on GaSb once the reaction of the As_2 with GaSb surface is suppressed. While the single As atomic layer seems to form on the Ga atomic layer by ambient As overpressure, it appears to lack long-range uniformity. This leads to a higher defect density than what can be realized in the compressive growth mode. To achieve the higher quality tensile GaAs epilayer on GaSb, a non-reactive atom can be used either as a surfactant or catalyst. A thin buffer of AlSb, with greater bond strength compared to GaSb, may also reduce the As/surface reactivity enabling long-range uniform IMF formation. Therefore, control of both tensile (GaAs on GaSb) and compressive (GaSb on GaAs) can lead to new devices based upon the novel integration schemes.

The IMF growth mode has also been applied for obtaining high quality III-Sb epilayers monolithically on Si substrate. We demonstrated that the IMF array in the growth of highly mismatched ($\Delta a_0/a_0$=13%) AlSb bulk layers can be formed on both of Si (100) and 5° miscut Si (100) substrates. Moreover, a 5° miscut Si (001) substrate can provide the effect of suppress of APDs. Under the optimized growth conditions, strain energy from the AlSb/Si interface is accommodated by a self-assembled 2D array 90° of interfacial misfit dislocations resulting in very low defect density and the suppression of APDs. We attribute the success of AlSb growth on Si surface to both the step doubling-atom mechanism in combination with the strong Al-Sb atomic bond. The AlSb bulk materials with low dislocation density and strain-relieved properties generated by the growth conditions can provide a promising technology for the monolithic integration of III-V devices on Si substrate.

Finally, We have demonstrated the ability to control either an IMF or a SK growth mode to grow GaSb QDs on GaAs substrates by varying V/III ratio. A high V/III ratio such as 10:1 produces IMF growth mode, while a low V/III ratio of 1:1 favors SK growth mode. The experimental results indicate that low V/III ratio has the effect of suppressing Sb segregation, which produces smooth morphology and low defect density, while a high V/III ratio results in high Sb segregation, rough morphology at the interface, and threading dislocations.